applied sciences

MDPI

Review

The BCL Method for DSSC: Basis and Applications †

Mauricio Barrera [1,*], Irma Crivelli [2] and Barbara Loeb [1]

[1] Facultad de Química y de Farmacia, Pontificia Universidad Católica de Chile, Vicuña Mackenna 4860, Santiago 781000, Chile; bloeb@uc.cl
[2] Facultad de Ciencias, Universidad de Chile, Las Palmeras 3425, Santiago 6094411, Chile; icrivell@uchile.cl
* Correspondence: mbarrerh@uc.cl
† We dedicate this work to the memory of Professor Angelica Francois.

Abstract: In this work, a comprehensive view of the route that led to the construction of a theoretical approach to the functioning of DSSC is presented. The model was developed based on the theoretical interpretation of experimental results obtained along the years for solar cells including different dyes. This allowed the authors to generate the Barrera, Crivelli, Loeb (BCL) model. The method is based on a system of equations that uses time-dependent density functional theory (TDDFT) calculations to obtain a theoretical index, the Global Efficiency Index (GEI), for the efficiency of a sensitized solar cell. The GEI is obtained through the product of three factors: the available energy for injection, the amount of charge injected, and the efficiency of regeneration. The results so far obtained show a promising correlation with the experimental index of photo conversion efficiency (PCE). Moreover, the method provides theoretical tools that allow us to obtain an understanding of the operation of the cell, and provide us with the keys to optimize it. Its application to other type of devices, as, e.g., the highly more efficient perovskite solar cells, emerges as a challenging future goal.

Keywords: DSSC; solar cells; perovskite; BCL

check for updates

Citation: Barrera, M.; Crivelli, I.; Loeb, B. The BCL Method for DSSC: Basis and Applications. *Appl. Sci.* **2022**, *12*, 2358. https://doi.org/10.3390/app12052358

Academic Editors: Laura Ciammaruchi and Sang Hyuk Im

Received: 25 November 2021
Accepted: 7 February 2022
Published: 24 February 2022

Publisher's Note: MDPI stays neutral with regard to jurisdictional claims in published maps and institutional affiliations.

Copyright: © 2022 by the authors. Licensee MDPI, Basel, Switzerland. This article is an open access article distributed under the terms and conditions of the Creative Commons Attribution (CC BY) license (https://creativecommons.org/licenses/by/4.0/).

1. Introduction

At beginning of 1991, Brian O´Reagan and Michael Graetzel published in *Nature* [1] their pioneering work on the development of a low-cost solar cell based on dye-sensitized colloidal films (DSSC) [2]. The device showed an impressive 7.1% yield. The photo electrochemical cell is built with a photo anode, based on a conductive glass covered with a Titanium Dioxide thin film that in turn is over coated with a ruthenium dye. Figure 1a displays the main photo physical processes occurring during one operative cycle of the cell. The dye, by means of its metallic center, is able to capture one photon from visible sunlight. The absorbed energy permits the generation of a metal ligand charge transfer (MLCT)-excited state (1), where the electron can be injected to the conduction band of the semiconductor (2) and then, by means of an external circuit, generate electric work (3). The cycle is closed when the electron returns to the cell through the cathode, reduces the electrolyte (4), that in turn regenerates the oxidized dye (5) and starts a new photo cycle. Processes (6) and (7) are the deactivating competitive mechanisms through which the efficiency of the cell is reduced. This promising result invited researchers to participate in a race to design and synthetize new champion dyes by modifying their molecular structure, starting with the N3 dye shown in Figure 1b; further studies led to the design of a panchromatic sensitizer, the black dye (BD) with an 11.1% of certified yield [3]. A further improvement, taking the total yield to about 15.5% in DSSC was achieved by introducing cell modifications; in addition, the use of perovskites in solar cells has permitted to increase the yield to values higher than 25% [4].

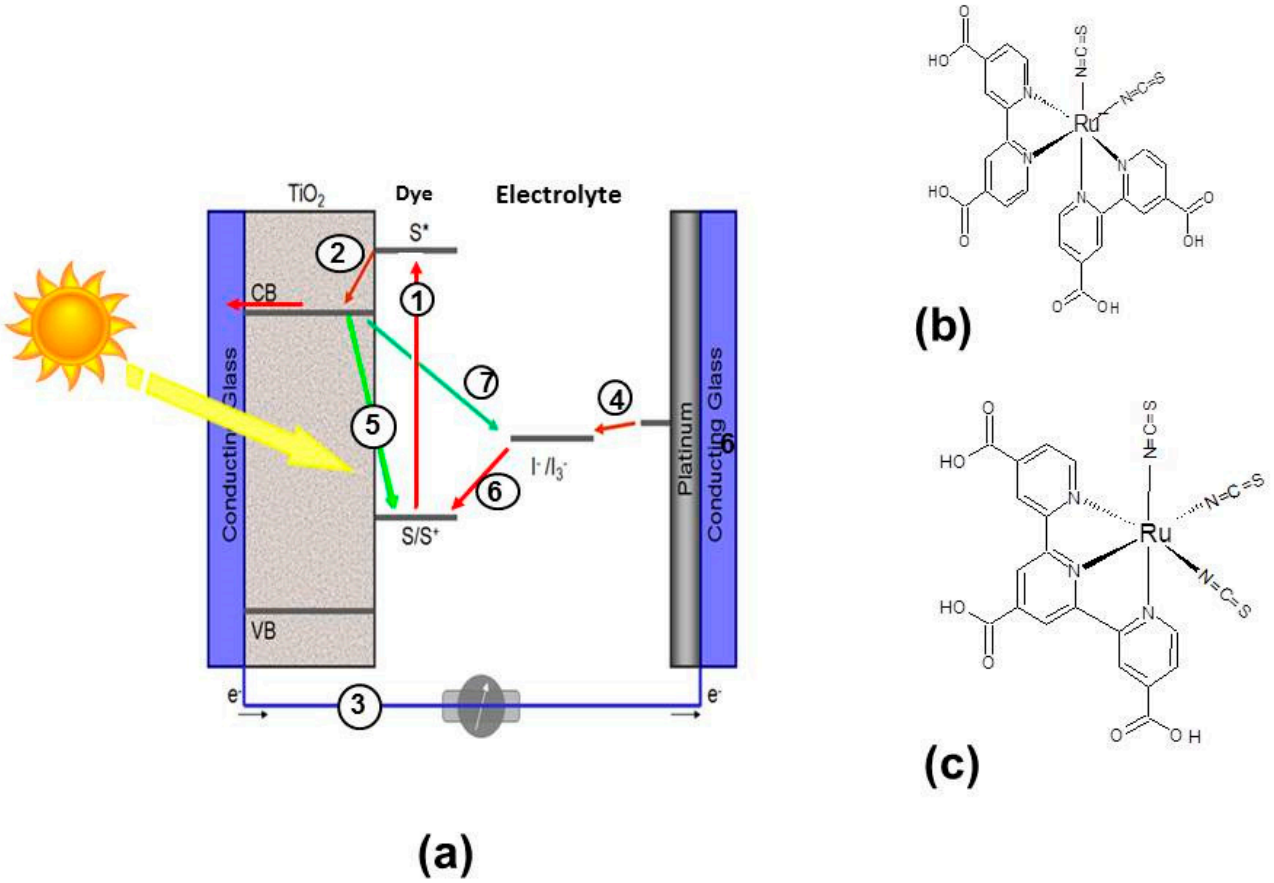

Figure 1. (**a**) Schematic representation of a DSSC device; (**b**) N3 dye; (**c**) BD dye.

For more than a decade, our group [5] has focused part of its research on the synthesis, characterization and theoretical description of new ruthenium complexes, with the aim to visualize the main factors responsible for an efficient electronic injection in a dye-sensitized solar cell (DSSC). The research has been centered around two topics: the nature of the anchor group and the enhancement of the optical properties by increasing the extinction molar coefficient, or by red shifting the absorption spectra. Different anchoring ligands were designed, and the corresponding ruthenium complexes synthesized. The electronic behavior of the complex, and its performance as dye for DSSC, was evaluated by different experimental techniques, as well as by DFT calculations. The experimental information was collected, analyzed together with data from the literature, and interpreted to build a theoretical model that could explain the results and provide reasonable guidelines for designing new ligands and complexes in the future.

This review shows the route that led to the construction of the BCL model, a theoretical approach that quantifies the efficiency of a given dye through a theoretical index, GEI, the Global Efficiency Index (ξ). This parameter is parceled in three main contributions: light harvesting, electron injection and regeneration.

As a first step, theoretical calculations were planned to study the excited state of several acceptor polipyridinic ligands. The ligands were analyzed by fragments, in order to understand how the different parts of the molecule contribute to the acceptor capacity observed for them.

Having applied the fragment decomposition of ligands, this concept was employed to model the electronic transitions in the absorption spectra of the corresponding complexes. The electronic transitions were considered as a sum of single electronic excitations occurring between the different fragments of the molecule. In this sense, it became feasible to identify

excitations as intraligand (IL), ligand to ligand (LL), metal to ligand (ML), and ligand to metal (LM).

Furthermore, and in order to understand the anchor group properties, based on the previously described analysis, the 'it' parameter was defined for the first time. It represents the amount of absorbed energy that is delivered to a specific fragment, in this case the anchor group. Using this parameter, the suitability as anchor of several moieties such as carboxy, ester, cyano and hydroxy could be evaluated.

Finally, with the experimental and theoretical information collected, and based on the conceptual pattern described, the BCL model was built. It focuses on three parameters: available energy for injection (F1), the amount of charge injected (F2), and the effectiveness of regeneration (F3). It permits us to gain an understanding of the IPCE and the behavior of the efficiency in a series of ruthenium-based dyes.

As mentioned earlier, it is the purpose of the present work to present the way in which the BCL method was constructed and its theoretical basis. In the different chapters, its application to series of ligands and complexes, was developed, testing its capacity to reproduce experimental data. In this process, only ligands and complexes already published, and therefore satisfactorily characterized by conventional techniques, were considered. The reference where this information appears was included in each chapter.

2. Materials and Methods

2.1. Materials

Ligands and complexes were synthesized and characterized as described in references [6–8].

2.2. Methods

Free radicals were generated by electrochemical reduction in the cavity of an EPR instrument and simulated spectra were generated using standard software. Theoretical calculations were performed with the ADF package [9].

3. Mapping Electronic Density in the Ligand Excited State

In order to build suitable dyes for dye-sensitized solar cell (DSSC) devices, a series of quinone-derivatized polypyridinic ligands with an acceptor character were designed [6]. The hypothesis was that the acceptor ligand in the complex should meet some basic requirements such as (a) bidentate (N, N)-type coordination to the metal, (b) the possession of planar geometry and (c) enhanced electron acceptor character. The ligands studied, shown in Scheme 1, were 12,17-dihydronaphtho-[2,3-h] dipyrido [3,2-a:2^0,3^0-c]-phenazine-12,17-dione, Aqphen, dipyrido[3,2-a:2^0,3^0-c]benzo [3,4]-phenazine-11,16-quinone, Nqphen, and uracil(5,6-diamino-1,3-dimethyl), Pptd.

These ligands are rather planar, with the exception of pptd, and can be visualized as having a bidentate (N, N) phenanthroline-type coordination center fused to a pyrazine or phenazine portion. Their difference lies in the type and relative position of the corresponding quinonic groups. Based on these acceptor type ligands, different complexes can be built, containing other bipyridine-based bidentate ligands. Figure 2 shows that after receiving an electron, by direct reduction or by MLCT (metal–ligand charge transfer) excitation, the acceptor ligands in the complex should behave as a "three step cascade" with a π^* ordering level following π^* (phenanthroline) > π^* (phenazine or pyrazine) > π^* (quinone portion).

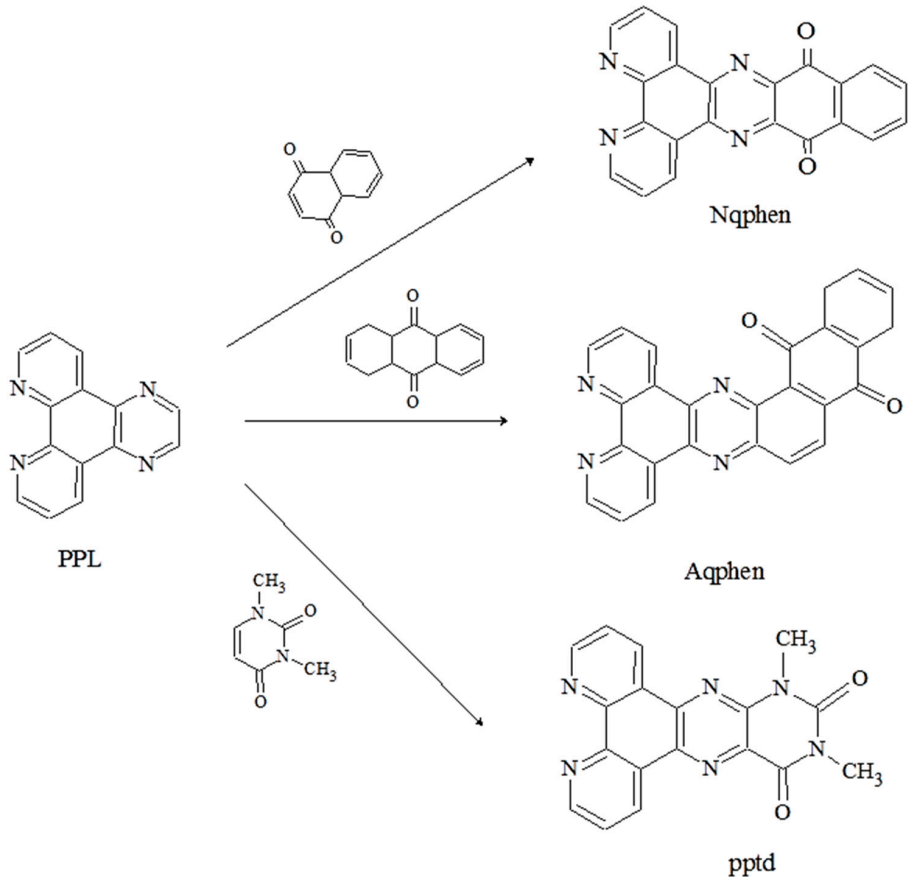

Scheme 1. Decomposition of polypyridinic ligands in term of fragment components.

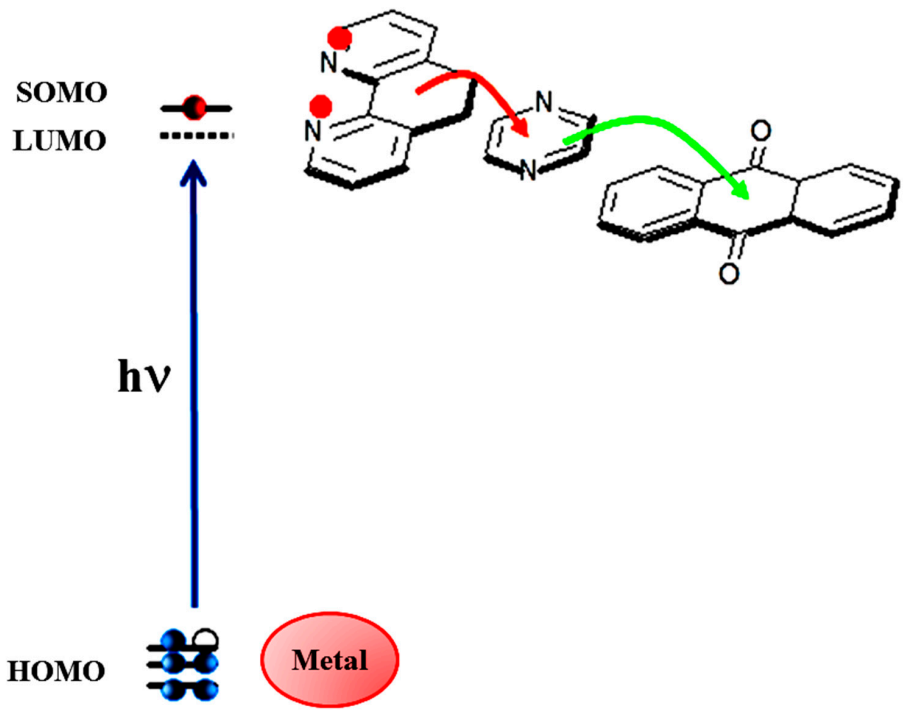

Figure 2. The excited state redistribution of the electronic density after the excitation from the ground state to the metal ligand charge transfer acceptor.

The ligand ppl was also studied as a model, considering that it represents the unsubstituted fragment (Scheme 1) that can be modified by introducing three kinds of fragments containing quinonic groups: naphtoquinone, anthraquinone and dimethyl pyrimido quinone.

One way to predict if the requirements mentioned above are present in a specific ligand is to study the nature of the lowest unoccupied molecular orbital (LUMO), which reflects the electron withdrawing capacity and the electronic distribution in the acceptor state. However, this is a virtual orbital and, hence, it cannot be accessed experimentally. This shortcoming can be overcome by adding a single electron to this empty level by means of an electrochemical reduction in the neutral molecule, giving rise to the single occupied molecular orbital (SOMO). The SOMO can be examined by two complementary approaches: one experimental, involving the reduction in the ligand and the subsequent analysis of the ESR pattern and hyperfine coupling constants, and the second is theoretical in nature, involving the calculation of suitable theoretical descriptors measuring the acceptor power and the delocalization of the unpaired electron along the molecular skeleton. The theoretical results would enable a picture of the acceptor state and to be constructed and correlated with the experimental data.

3.1. Theoretical Background

In the literature, the introduction of numerical parameters called "descriptors" has been used for the study of chemical reactivity. These parameters can be global or local. The global descriptors consider the molecule as a whole, while the so-called local descriptors explain the role of specific sites in the chemical skeleton, helping in this way to understand the selectivity when used in chemical reactions.

As the focus of the present study was to understand the effect of a quinonic group in the acceptor capacity of the ligand, and how an added charge would distribute along the corresponding ligand, the introduction of global and local descriptors was considered for the first time in DSSC dyes. Specifically, a global descriptor, the electrophilicity [10], a measure of the acceptor power of the neutral ligand, and the Fukui function [11], a local descriptor that shows how the spin density of the formed radical is distributed on the whole molecule, were used. A brief description of both parameters is given below.

The capability of a ligand to accept one electron is measured by its electron affinity. However, if only partial electron transfer occurs, it is necessary to define a property considering the maximum electron flow that would lower the total binding energy. The total capacity for accepting charge of the molecule is identified with the electrophilicity index E^+:

$$E^+ = \frac{\mu^2}{2\eta} \tag{1}$$

By considering Koopmans theorem for vertical excitations, the ionization potential can be estimated by the energy of the HOMO orbital, while electron affinity is related to the negative of the LUMO.

Since the electrophilicity index is a global quantity giving information about the whole molecule, it is necessary for our ultimate purpose to specify how the accepted charge will be distributed along the different atoms of the molecule. This can be achieved by introducing a local descriptor, f_α, like the Fukui function, for a radical,

$$f_\alpha = \rho_{s\alpha} = \rho_\alpha(\uparrow) - \rho_\alpha(\downarrow) \tag{2}$$

where $\rho_{s\alpha}$ is the spin density on atom α obtained through a Mulliken's population analysis; it is subject to a normalization condition $\sum_\alpha f_\alpha = 1$ by setting $\rho_\alpha(\uparrow) = \rho_{SOMO}$ and $\rho_\alpha(\downarrow) = \rho_{HOMO}$; the $\Delta\rho = \rho_{SOMO} - \rho_{HOMO}$ difference is also a measure of the Fukui function for a single excitation. It is noteworthy that, for the case of a radical with an unfilled shell, the Fukui function is defined as the response of the electronic density to a change on the spin polarization.

All theoretical calculations were performed with the ADF package.

3.2. Results

Cyclic voltammetry measurements were carried out for the four ligands, permitting us to determine the corresponding reduction potentials. The results obtained are displayed in Figure 3a together with the calculated energy of the SOMO.

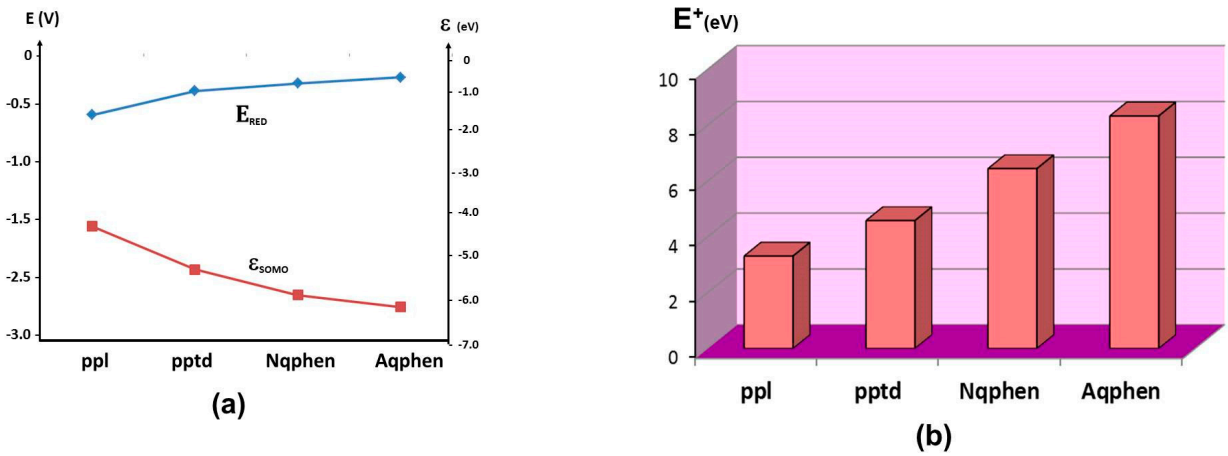

Figure 3. (**a**) Values for the reduction potentials of the ligands, and for the calculated energy of the SOMO. (**b**) Electrophilicity Index.

When compared to ppl, it can be seen that the introduction of a quinone group diminishes the reduction potential in different extents, with aqphen the most easily reduced. Looking to the SOMO-calculated energy a contrasting tendency is observed, confirming that the ligand with a higher electron affinity is the one with a lower reduction potential.

The calculated electrophilicity index, displayed in Figure 3b, shows that quinonic groups increase the acceptor capacity of the polypirydinic ligands, especially in the case of nqphen and aqphen, which possess the higher capacity to accept electronic charge.

In a second series of experiments, the free radicals of the five ligands under study were prepared "in situ" by electrochemical reduction in the cavity of an EPR instrument. In parallel, simulated spectra were generated using standard software [12]. The potential applied corresponded to the one observed for the first monoelectronic wave obtained from the cyclic voltammetric experiments. The signal of the free radical obtained was registered and the coupling of the unpaired electron with N and H nucleus measured through the calculation of the hyperphyne-coupling constants. According to these values, a simulated ESR spectrum was generated, as shown in Figure 4a.

Figure 4b displays the nucleus that interacts with the unpaired electron according the EPR data, and Figure 4c shows the Fukui function, for the different fragment components. For the simple case of ppl, according to EPR, the spin density is localized on the nitrogen and on the carbon skeleton of the phenanthroline and pyrazine fragments.

On the other hand, the Fukui function shows changes in the spin density of the nitrogen and carbon atoms of pyrazine, while for phenanthroline only, carbon atoms are affected. In nqphen, the ppl ligand is coupled with a naphtoquinone group. In this case, the EPR spectrum displays only one signal: the free electron does not interact with nitrogen or carbon. The Fukui function reveals that the electron density is localized mainly on the carbon and oxygen atoms of the quinonic group.

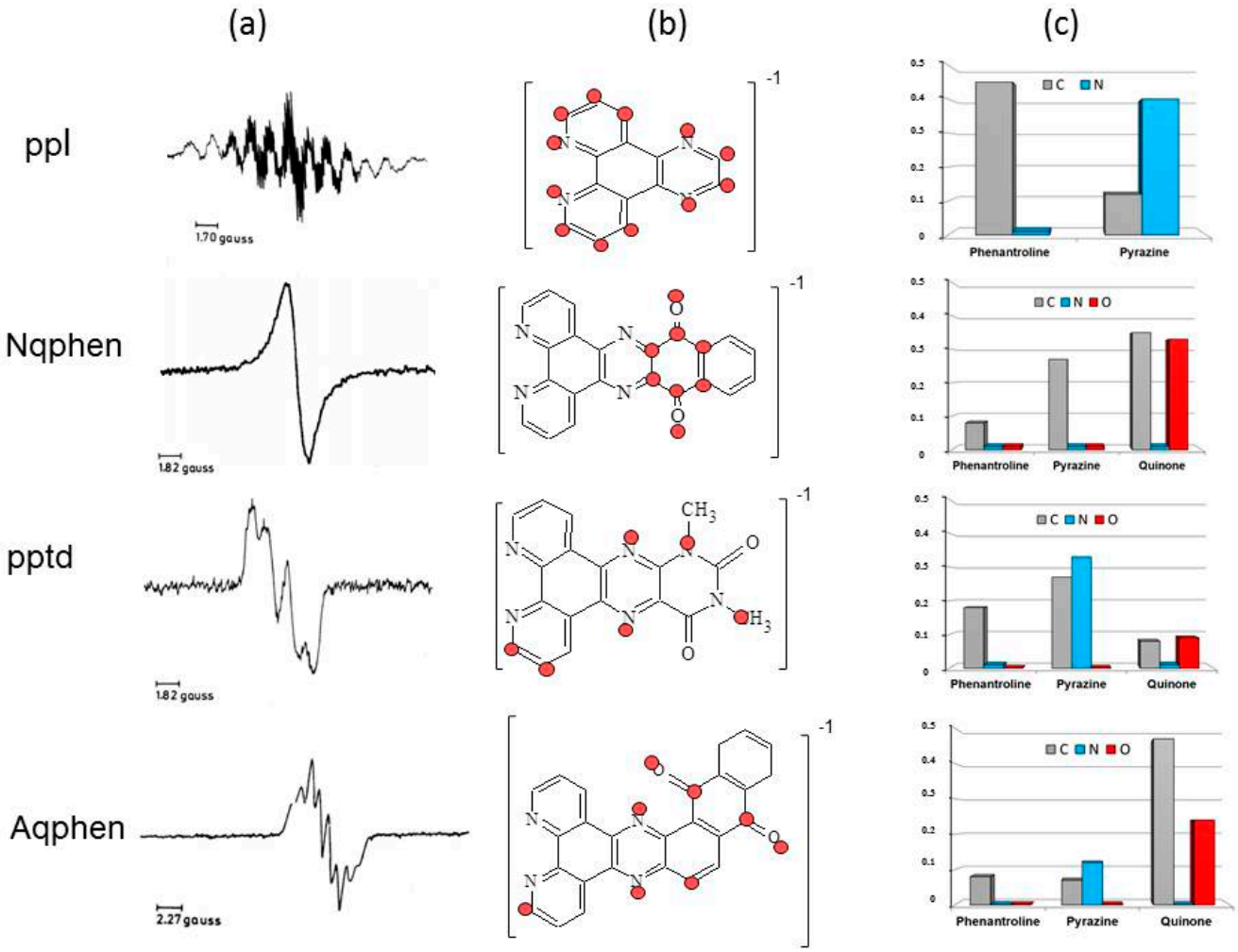

Figure 4. (**a**) Simulated ESR spectrum of the free radicals of the ligands, prepared "in situ" by electrochemical reduction in the cavity of an EPR instrument. (**b**) Nucleus which interacts with the unpaired electron according the EPR data. (**c**) The Fukui function, Equation (2), for the different fragment components.

For the pptd ligand, the quinone moiety is in *meta* position instead of *para*, as in nqphen. This structural change is reflected in the EPR spectrum: the Fukui function for this ligand shows a high value for the pyrazine fragment, with contributions from carbon and nitrogen atoms. It is interesting to note that the change in the relative position of the quinone groups caused the charge to be redirected and stored on the nitrogen atoms of pyrazine.

As a whole and looking at the above results, the effect of the quinonic group in increasing the electron acceptor capacity of the ligands is evidenced. Additionally, it can be concluded that the electronic distribution is different depending on if the quinone groups are located in *meta* or *para* positions: in aqphen and nqphen, the highest electron density is in the quinonic part. This is clearly reflected by the first reduction potential that appears at less negative potentials and the increasing value of the electrophilicity.

4. A Big Challenge: Understanding the Absorption Band of Ruthenium Dyes

It has been proposed [13] that one of the requirements for a good yield in DSSC is the directionality of the charge distribution in the excited state, produced by dye light absorption. For the electron injection process in the solar cell, metal-to-ligand charge transfer bands (MLCT) appear to be more effective, due to their directionality, than intraligand (IL) or π–π* bands. When tested in solar cells, ruthenium polypyridinic dyes with extended π

systems show an enhanced light-harvesting capacity that may or may not be reflected in a high collected electrons/absorbed photons ratio.

In published articles concerning ruthenium complexes with chromophoric polypyridinc ligands, the assignment of the nature of the visible absorption band is not conclusive, given that the intraligand band could experience a bathochromic shift and approach, or even surpass, the MLCT band position.

Focusing on the assignment of the absorption bands and the nature of the emitting state, the aim of this study [7] is to elucidate if all the absorbed photons of these dyes are potentially useful in the generation of electric current. To achieve this goal, a series of four ruthenium complexes with 4,40-distyryl-2,20-dipyridine (LH) and 4,40-bis[p-(dimethylamino)-R-styryl]-2,20-bipyridine (LN) "chromophoric" ligands (Figure 5) was studied.

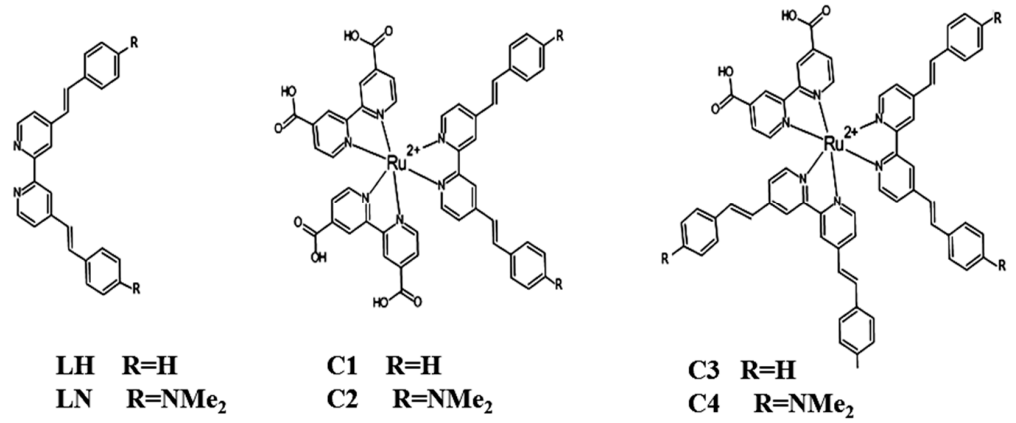

Figure 5. General Structure for unsubstitued (R = H) and substituted (R = NMe_2) Chromophoric Ligand (LH, LN) and Ruthenium Complexes. C1: $[Ru(bpy(COOH)_2LH]^{2+}$; C2: $[Ru(bpy(COOH)_2(LNMe_2)]^{2+}$; C3: $[Ru(bpy(COOH)(LH)_2{}^{2+}$; C4: $[Ru(bpy(COOH)(LNMe_2)_2]^{2+}$.

The observed experimental results were complemented with TDDFT calculations to elucidate the nature of the absorption bands, and a theoretical model was proposed to predict the available energy that could be injected from their singlet or triplet excited states.

Spectroscopic and electrochemical experimental studies were made for the complexes shown in Figure 5, and are described in what follows. Their results were used as a base for the theoretical calculations.

4.1. Results

4.1.1. Absorption Spectra of Ligands

Absorption spectra of the chromophoric ligands LH and LN show a broad and intense band centered at 317 and 390 nm, respectively, as can be seen in Figure 6, where results from TDDFT calculations on the gas phase, performed with the ADF pacakage, are also displayed.

The absorption bands of ligands LH (λ_{max} = 317 nm, ε = 90,000) and LN (λ_{max} = 390 nm, ε = 80,000), can be atributed at first to an MLCT process, which appears to be displaced by lower energies when compared to bipyridine (λ_{max} = 280 nm). This red shift has been attributed to the presence of the aromatic π-conjugated system. The effect is enhanced in the LN ligand, due to the presence of the electron-donating aminoalkyl substituent. An ILCT contribution [14–17] to the absorption can also be expected. The addition of a small amount of acid to a solution of the ligand diminishes the intensity of the 390 nm band, probably due to the protonation of the amino group which, therefore, can no longer participate in the ILCT transition. This experimental test supports the possibility of an ILCT contribution.

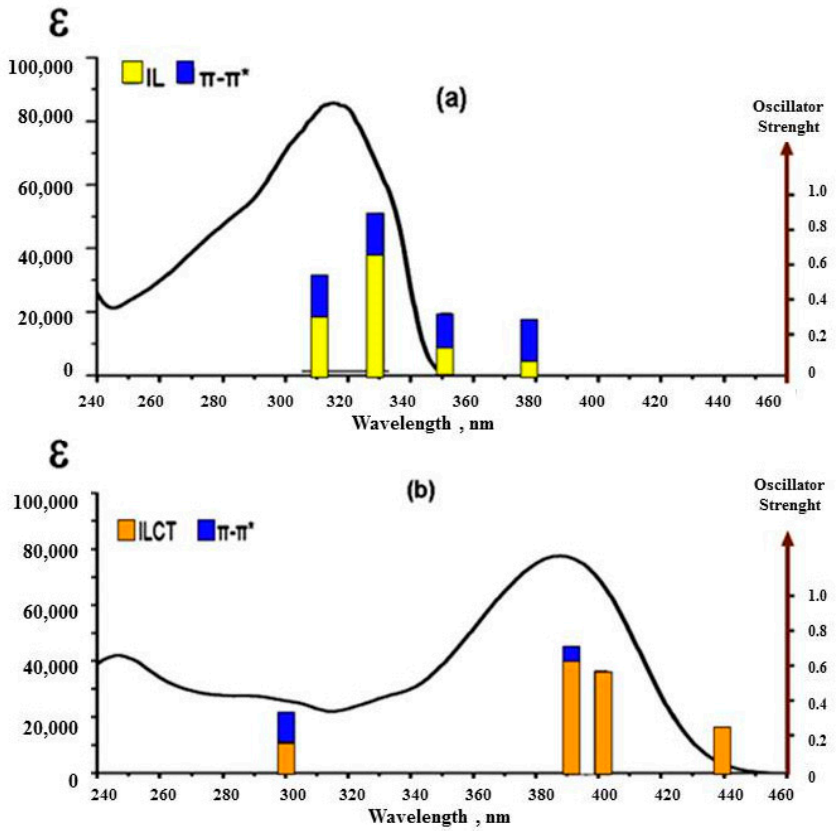

Figure 6. Experimental absorption spectra of (**a**) LH and (**b**) LN ligands in acetonitrile solvent. TTDFT-corresponding calculations are shown in bars.

A theoretical analysis combining TDDFT calculations with a molecular orbital description, in terms of the three-fragment composition of the ligand, allows us to understand the nature of the observed band. If the fragments are called F (phenyl), V (vinyl) and P (piridyl), it becomes possible to assign an intraligand (IL) character of an excitation when the charge density is displaced from the FV fragment to the P fragment. A π–π* character in an excitation from V to V, and an intraligand charge transfer character (ILCT) to an excitation started on the amino substituent of the F fragment and ended on the bipiridyl group. Applying this approach to the experimental results, it follows that the LH absorption spectra contains a sum of IL + π–π* electronic transitions, while the LN ligand is mainly composed by ILCT excitations.

The three processes depicted in Figure 7 also represent three types of electronic displacement of the electronic cloud that surrounds the carbon skeleton of the mentioned polypiridinic ligands. For the first case (IL), electronic density localized on the FV fragment moves parallel along the XY plane to the bipyridine empty π* orbitals through a process that can be assimilated to a simple deformation of the electronic density. The intraligand charge transfer process shares some characteristics with the IL since it also occurs along the XY plane, ending in the P fragment. However, they differ in terms of the origin of the excitation; for the case of ILCT, is the origin is located in atomic orbitals of the amino substituent in the F fragment. As a consequence of this electron transfer, an induced dipole moment is created along the molecule axes.

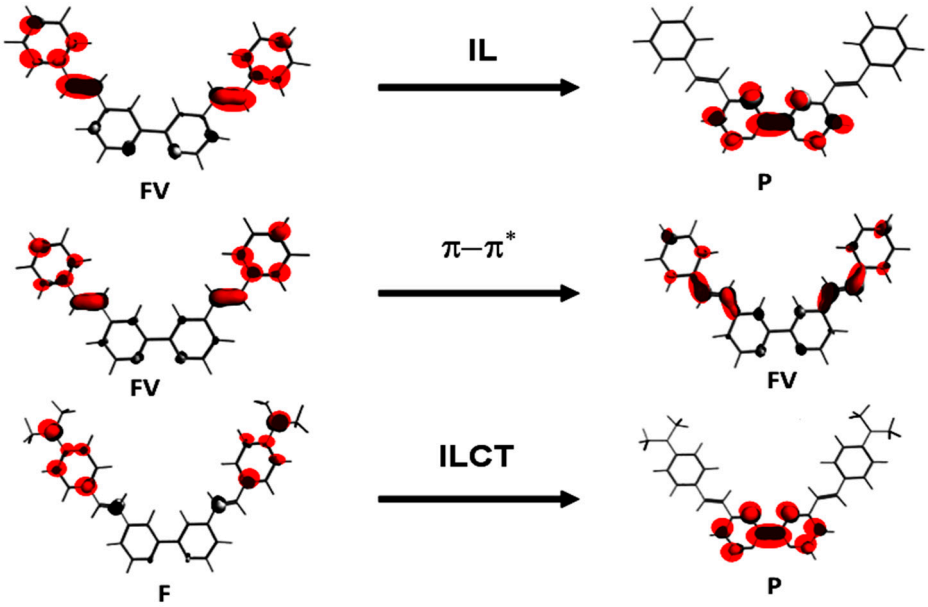

Figure 7. Types of electronic transition ocurring wihin the diferents fragments of LH and LN ligands. (IL: intraligand; ILCT: intraligand charge transfer.)

The electron transition, occurring within the FV fragment, involves mainly π and π* molecular orbitals of the vinyl fragment. This excitation occurs parallel to the z axis and perpendicular to the molecular plane. Looking to their directionality, both IL and ILCT occur in the same plane, while π–π* are perpendicular to them. ILCT provide greater directionality than IL, due to the induction of a change in the dipole moment of the molecule.

4.1.2. Absorption Spectra of Complexes

The absorption spectra for the ruthenium complexes studied in this work show two characteristic bands: The first appears in the UV region and shows high ε values. This band can be associated with the described absorbance of the chromophoric ligand (LH or LN), although red shifted due to the effect of coordination to the metallic center. The second broad and less intense band is located in the visible region and, according to the literature is mainly assigned to an MLCT band, also considering the fact that it appears at lower energy. Regarding solar cell devices, the second band is more relevant in the injection process and, therefore, is interesting to analyze. Additionally, since the energy absorbed comes from the visible region, it could be expected that modifications of the structure of the complexes should result in a change of the energy and intensity of the band, allowing us to improve the solar cell device.

A summary of their electrochemical and optical properties of C1–C4 complexes is shown in Table 1.

The results displayed in Table 1 enable these complexes to be characterized. It can be highlighted that complexes C1–C4 exhibit enhanced absorption capacity, possessing a broad absorption band in the visible region with a high extinction molar coefficient in accordance with the proposed original design. However, in the hypothetical case that most of the absorbed energy could be delivered to the semiconductor, the injected energy should relate directly to the amount of absorbed energy and, therefore, depend on the molar extinction coefficient.

Using this parameter as a predictor index, the set of complexes can be ordered in the following way: C4 > C3 = C2 > C1, where C4 should be the most suitable for DSSC. This crude prediction needs to be examined with more detail, and it becomes necessary to

disclose the nature of the absorption bands. For example, MLCT absorption that displaces electronic density to the ligand should be more relevant in DSSC than ILCT absorption.

Table 1. Electrochemical and UV–Vis absorption data for C1–C4 complexes.

Complex	Oxidation $E_{1/2}$/V	Absorption λ_{max}/nm ($\varepsilon/10^3$ M^{-1} cm^{-1})	Assignment	Emission λ_{max}/nm
$[Ru(bpy)_3]^{2+}$	1.28	310 (80) 474 (18)	ILCT MLCT	620
C1 $[Ru(bpy(COOH)_2LH]^{2+}$	1.11	349 (43) 473 (24)	ILCT MLCT	629
C2 $[Ru(bpy(COOH)(LH)_2]^{2+}$	0.97	329 (92) 486 (35)	ILCT MLCT	664
C3 $[Ru(bpy(COOH)_2LN]^{2+}$	0.48 1.15	370 (41) 486 (35)	ILCT MLCT	-
C4 $[Ru(bpy(COOH)(LN)_2]^{2+}$	0.46 1.23	426 (67) 480(63)	ILCT MLCT	-

To achieve this goal, a theoretical methodology was developed, based on TDDFT calculations combined with a transition density analysis (TDA), which allowed the participation of the different types of electronic transitions (ILCT, MLCT, LL, IL) to be quantified within the absorption band.

The first step of the proposed methodology consisted of expressing the composition of the molecular orbitals as the sum of several fragments, labeled Ru, LH, LN and Bp according to their main component, as shown in the energy diagram of molecular orbitals in Figure 8.

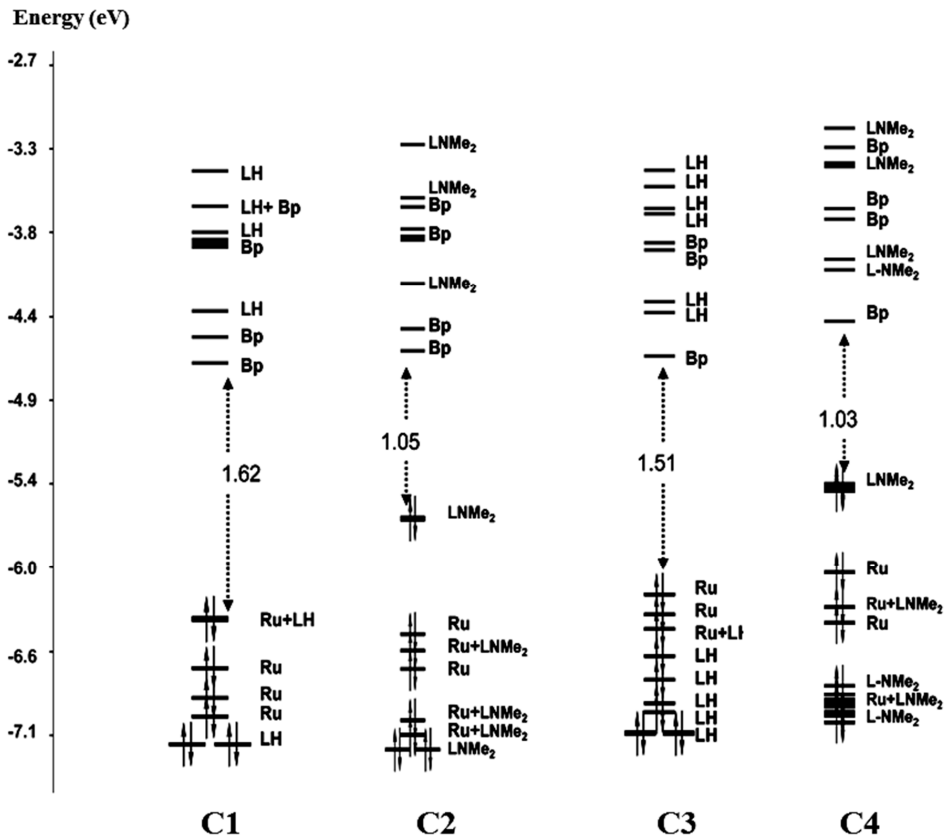

Figure 8. Molecular orbital energies and their composition in terms of basic fragments: Ru, LH, Bp and $LNMe_2$.

The theoretical MO calculations show consistency with the electrochemical experimental results for the complexes (Table 1). It is noteworthy that a correlation coefficient of 0.95 was found when comparing the first electrochemical oxidation potential with the calculated energy of the HOMO orbital for the series of complexes under study. This relationship opens the possibility to employ theoretical information to gain insight on the trend of electrochemical experimental results.

From the results in Figure 8 and Table 1, the assignment of the irreversible oxidation process to the amino group can be corroborated as complexes 2, 4 possess a HOMO orbital, related to the first oxidation, centered on the dimethylamino group. The same result is obtained by a fragment analysis performed for complexes C1 to C4, in an analogous way as described before for the free ligands.

In C1, the first five occupied MO of higher energy contain d pure orbitals and mixture of d orbitals with orbitals from the chromophoric ligand. The HOMO energy varies between −6 and −6.5 eV, showing two nearly degenerated ligands, one centered on the metal (orbitals d) and the other a mixture of d orbitals with π orbital from the chromophoric ligand. The composition is similar for all the complexes with LH ligand independent of the substituent of the bipyridine ligand

The first six unoccupied orbitals are dominated for the LUMO's of the bipyridine ligands and the chromophoric ligand. Electronic density analysis shows that the LUMO is localized in the P fragment of the chromophoric ligand. Otherwise, the LUMO + 1 (0.11 eV higher in energy) is localized on the bipyridine ligand. In complexes 1 and 3, the LUMO is centered in the bipyridine ligand that presents a lower energy than that of the chromophoric ligand LH.

When the dimethylamino substituent is introduced in complexes 2 and 4, the HOMO energy raises above −5.8 eV as a consequence of the competition between the electron-attracting effect of the substituted bipyridine and the effect of the electron–donor substituent on the chromophoric ligand. The electron density distribution of the HOMO is also altered, being principally located on the F fragment of the chromophoric ligand. The HOMO–LUMO gap is reduced about 40% in these complexes, in comparison to the corresponding complexes with no amino substitution.

4.1.3. Transition Density Analisys (TDA)

The forthcoming analysis is based on the existence of a transition state that originates in the Franck Condon excitations that populate a series of unoccupied molecular orbitals before thermal deactivation occurs. This set of LUMO orbitals are used to build the excited state electronic density (ϱ_T) and were generated when electrons from the ground state (ϱ_{GS}) are excited and jump to empty orbitals (ϱ_l) of the virtual state. These molecular orbitals combined together, form the transition density (ϱ_T) that contains the information of how electron density on the excited state is distributed on the molecular fragments (g_k)

$$\rho_T = \sum_{\text{lumo}} d_l \rho_l \tag{3}$$

$$\rho_l = \sum_j c_{lj} g_j \tag{4}$$

$$\rho_T = \sum_k d_k g_k \tag{5}$$

By combining (4) and (5), it can be observed that the transition density is composed by a specific set of basic fragments satisfying the orthogonal condition

$$g_l \cdot g_k = 0 \text{ and } g_k \cdot g_k = 1 \tag{6}$$

From de experimental absorption spectra the gamma parameter can be obtained, that relates to the energy absorbed by the complex in the visible region (400–600 nm)

$$\Gamma = \int_{\nu i}^{\nu f} \varepsilon(\nu) d\nu \tag{7}$$

From TDDFT calculations, the absorbed energy (E_A) can be calculated by the sum of single excitations (Γ_λ) of the product energy at which the excitation occurs, $E_\lambda = h\nu$, multiplied by the oscillator strength (f_λ)

$$E_A = \sum_\lambda \Gamma_\lambda = \sum_\lambda f_\lambda E_\lambda \tag{8}$$

On the other hand, an electronic transition occurs when an electron from the ground state is excited to a molecular orbital of the virtual state. Frequently it occurs that many pairs of HOMO–LUMO orbitals, and not only one, are excited simultaneously: the set of HOMO is identified by ρ_{GS} and the set of LUMO by ρ_T.

Figure 9a shows that at some specific wavelength the process $\varrho_{GS} \rightarrow \varrho_T$ occurs and involves pairs of fragment groups from the ground state $\{g_\alpha\}$ that are linked with a fragment of the excited state $\{g_\beta\}$. This gives rise to a set of correlated pairs of fragments represented by $\omega(\alpha,\beta)$. Therefore, it is possible to define a set of basic processes containing specific combinations of molecular fragments, $\omega_0(\alpha,\beta) = \omega_0^{\alpha\beta}$, as shown in Figure 9b.

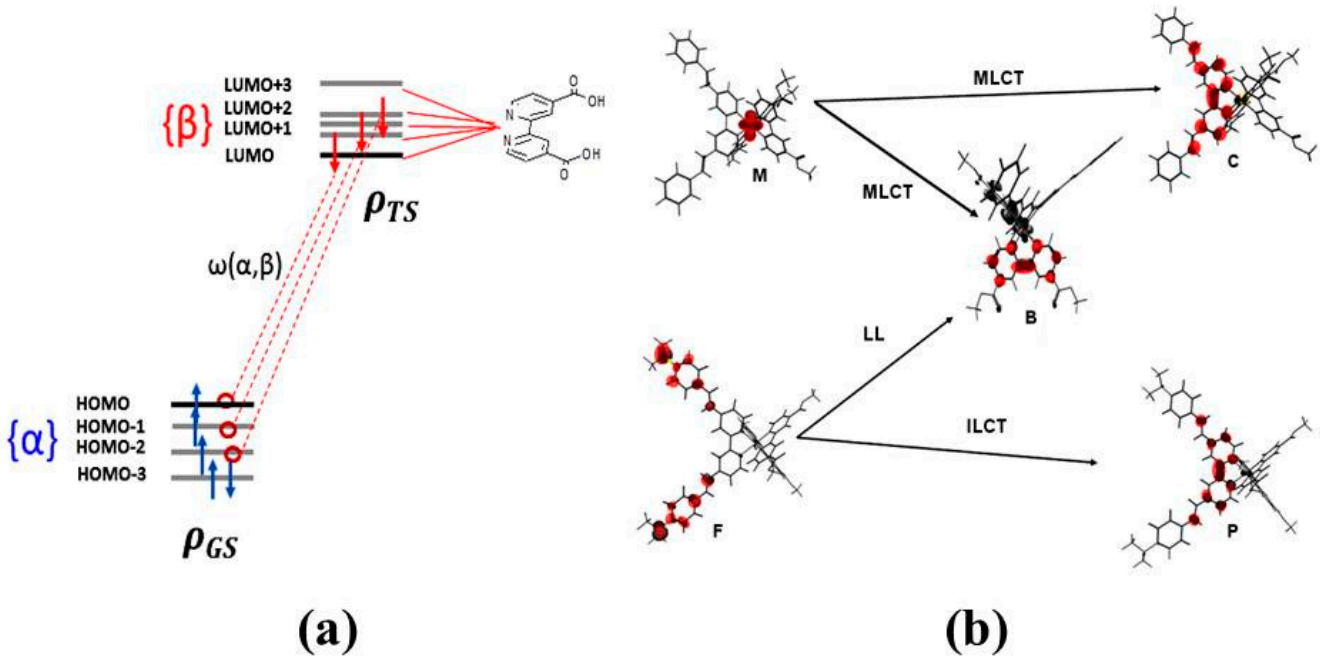

Figure 9. (**a**) ground state density ρ_{GS}, transition density ρ_{TS}, $\omega(\alpha,\beta)$ distribution function, $\{\alpha\ \beta\}$ molecular orbitals. (**b**) Possible electronic transitions: MB: MLCT band to the bpy carboxylate ligand; MC: MLCT band to the chromophoric ligand; LL transition; ILCT: intraligand charge transfer.

This figure shows that the electronic transitions MC and MB belong to the category of metal-to-ligand charge transfer, MLCT, and involve a charge transfer from the ruthenium atom (M) to the chromophoric ligand (MC) or to bipyridine (MB). The ligand to ligand (LL) transition corresponds to a charge transfer between the F-substituted fragment of the chromophoric ligand and bipyridine.

Finally, Figure 9 shows a charge transfer process that occurs inside the chromophoric LNMe2 ligand, which is classified as an intraligand process (ILCT). If the intraligand

process does not show clear charge transfer character, it is named as IL, as would be the case of complexes with the LH ligand.

From the absorption spectra an absorption occurring at wavelength λ can now be described as sum of single basic excitations according to,

$$\Gamma_\lambda = \sum_k d_k \omega_0^{\alpha\beta} \tag{9}$$

4.1.4. Analisys of MLCT Band

Figure 10 displays the experimental absorption of the four compounds under study. It also shows the decomposition of the broad absorption band in terms of the described possible components of the excitation process, detailed in Equation (7). Accordingly, complex 1 shows the participation of a mixture of MLCT and IL electronic transitions. The MLCT excitations for this chromophoric complex can be separated in two types, one of them related to a charge transfer from the ruthenium center to the Chromophoric ligand (MC), while the other is directed to the dicarboxibipyridine group (MB). For the case of C1, MB transitions are observed, but then a second LH ligand is present like in the C2 complex, MC excitations are predominant.

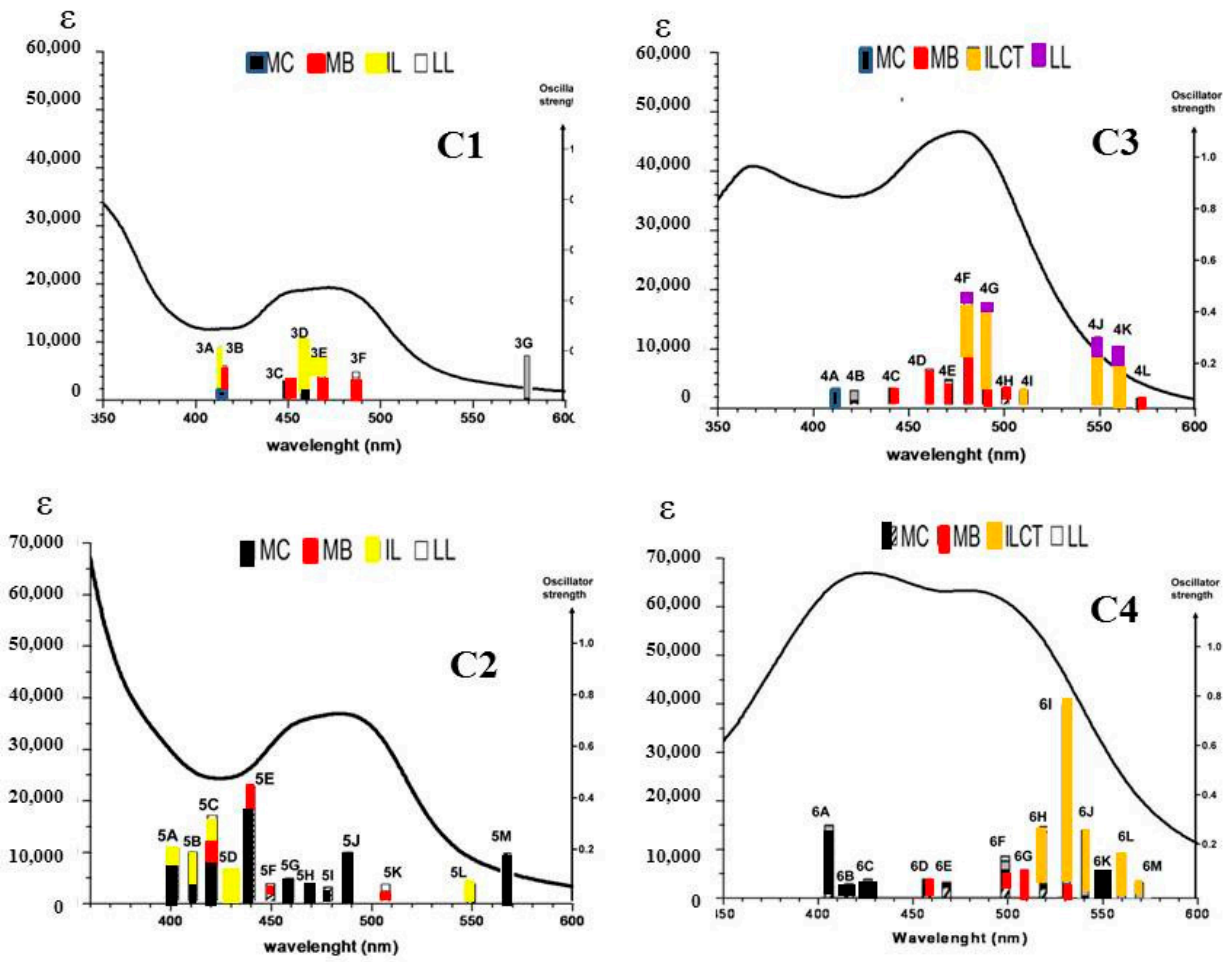

Figure 10. Experimental absorption spectra and calculated electronic transitions(bar) showing the participation of basic electronic excitations, MC, MB, IL, ILCT and LL.

On the other hand, looking at the complexes that incorporate the amino substituted ligands, it can be seen that in complex C3 MLCT excitations are present, accompanied by ILCT and LL contributions. The abundance of ILCT transitions increase when moving

to longer wavelengths. The same behavior is observed for the C4 complex, which shows falling-off in the contribution of MB excitations that is compensated by the presence of MC transitions.

The above analysis shows that the different absorption bands are a mixture of different types of excitations. In C1 and C2, MLCT and IL are predominant, while for C3 and C4, intraligand charge transfer transitions outweigh. It also can be mentioned that MLCT are found within the range of 400–480 nm and ILCT appear at longer wavelength.

As it was previously mentioned, each absorption is composed by a set of basic excitations, then the entire band can be described by a sum of them:

$$\Gamma = \sum_{\lambda} f_{\lambda}\, \Gamma_{\lambda} = \sum_{\lambda} f_{\lambda} \left(\sum_{k} d_k \omega_0^{\alpha\beta} \right) \tag{10}$$

Reorganizing and imposing the condition that $\sum_k d_k^* = 1$, Equation (9) is obtained

$$\Gamma = \sum_{k} d_k^* \omega_k^{\alpha\beta} \tag{11}$$

showing the decomposition of the absorption band in terms of single basic processes, with their percental contribution measured by the d_k^* coefficients. Figure 11 symbolizes the calculated values of these coefficients for each of the complexes under study.

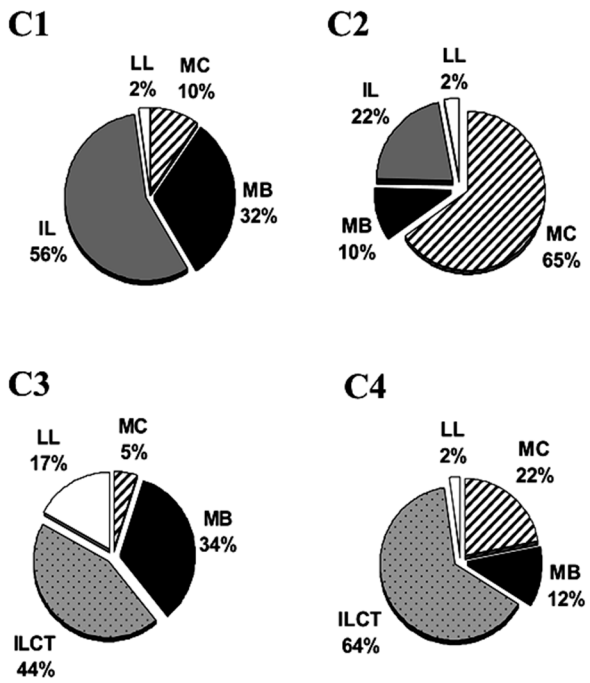

Figure 11. Participation of single basic excitations on the entire absorption band.

The above figure reveals that for C1 the absorption band comprised in the range of 400 nm to 600 nm is a mixture of 56% IL + 32% MB + 10% MC + 2% LL excitations. The introduction of a second LH ligand modifies the previous composition by enhancing the number of MC (65%) excitations, with the associated diminishment of IL and MB excitations. The amino substituent introduced in the chromophoric ligand C3 shows that ILCT and MB excitation predominate. At the same time, an increase in the contribution of LL excitations prevail respect to MC excitations.

Finally, in complex C4, the 64% of the aborbed energy is concentrated on ILCT excitation and 22% on MC excitations. In summary, employing the present framework, in combination with TDDFT calculations it is feasible to calculate the composition of the

visible bands and understand how its distribution changes by modifying the nature of the ligands.

Focusing on the application of this methodology to the development of solar cells, it is interesting to calculate how much of the absorbed energy is delivererd to the diferent fragments, and specifically to the B (carboxylate) fragments from where electronic injection to the semiconductor takes place. Therefore, a distribution function, *f(β)*, containing the relative participation of the different fragments is build. This function is defined through Equation (12):

$$f(\beta) = g_\beta \cdot \rho_T = k_\beta \tag{12}$$

Consequently it is possible to calculate the delivered energy to a specific fragment in the hot excited state through Equation (13)

$$E_D(\beta) = E_A f(\beta) \tag{13}$$

Calculated values for amount of the absorbed energy chanelled to the B and C fragments is displayed in Figure 12.

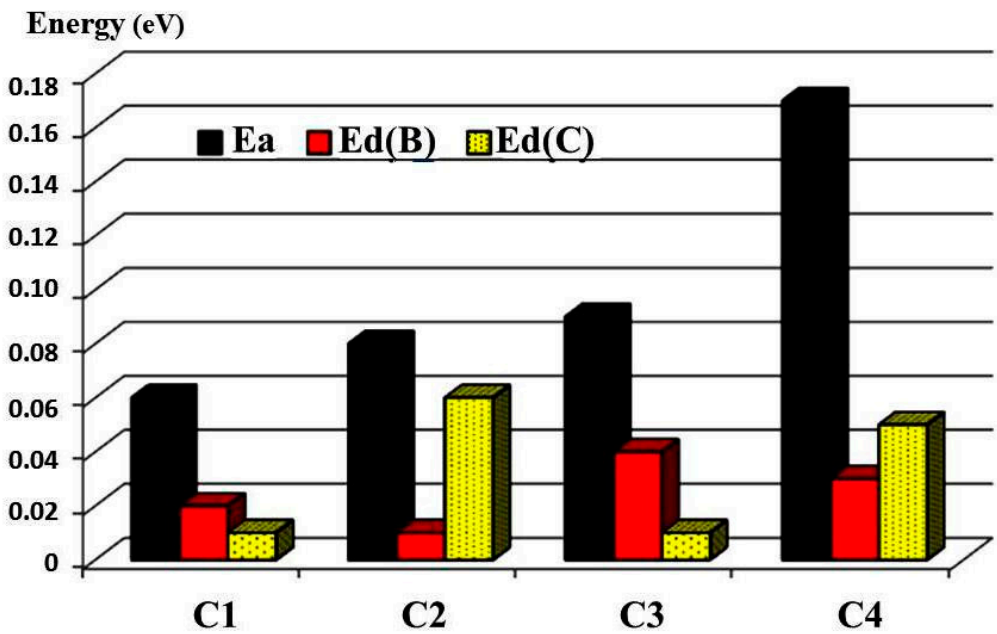

Figure 12. Comparison of absorbed energy (Ea) and the delivered energy (Ed) to the dicarboxybipiridine (B) and chromophoric (C) ligand for the four complexes.

Three interesting remarks can be obtained through the analisys of this figure. First, the absorbed eenergy increases with the number of chromophoric ligands coordinated to the metal center: C2 > C1 and C4 > C3. C4 has the higher capacity to absorb sunlight, the same conclution obtained before through the analisys of extintion molar coeficients. Nevetheless, interestingly, the amount of delivered energy to the dicarboxibipirydine group (B) is independent of the absorbed energy, while increasing the number of chromophoric ligands does not imply an increase in delivered energy to this fragment. The reason for this is that the chromophoric ligand compites with dicarboxibipirydine to concentrate absorbed energy. In this sense, the C3 complex appears to be the more effective.

4.1.5. Triplet State

The previous results represent the amount of electronic density concentrated on the anchor ligand that could be delivered to the semiconductor in accordance with the following photochemical process:

$$S_0 + hv \rightarrow S_n^* \tag{14}$$

$$S_n^* + TiO_2 \rightarrow S_0^+ + TiO_2\ (e) \tag{15}$$

Once the absorption process has been verified, the ruthenium complex is driven to a hot excited state where electronic injection occurs, previous to the non radiative decay. The electron transfer occurs through a possible transmitter–antenna mechanism, where the transmitter is located on the dicarboxibipyridine ligand and physically bonded to the surface of the semiconductor.

However, an alternative scheme can be derived by considering that thermal deactivation occurs and that the excited complex decays to the lower singlet, and then, by intersystem crossing, it reaches a long lived thermally equilibrated excited state (thexi) with a triplet character. It is from this thexi state that electronic injection should occur.

$$S_0 + hv \rightarrow S_n^* \tag{16}$$

$$S_n^* \rightarrow S_1^* \tag{17}$$

$$S_1^* \rightarrow T_1^* \tag{18}$$

$$T_1^* + TiO_2 \rightarrow S_0^+ + TiO_2\ (e) \tag{19}$$

In a second-row transition element, as in ruthenium, the triplet state can be populated from the singlet state given that the intersystem crossing yield; ϕ_{isc} is non zero for metals belonging to this series. In order to include the triplet state in the present framework, it is necessary to make a geometrical optimization of the molecular structure of the complexes in the triplet-excited state configuration. The intersystem crossing constant can be related to the amount of participation of the bypiridine fragment in the SOMO orbital of the excited state configuration.

$$\phi_{ISC} = \phi_T(B) = \varrho_{somo}(B) \tag{20}$$

Furthemore, the available energy for electronic injection I_T can be defined by:

$$I_T = E_D \phi_T(B) \tag{21}$$

which can be understood as the fraction of the delivered energy to the B fragment in the triplet state. Table 2 contains calculated values for the optimized geometry.

Table 2. Calculated values for the optimized geometry of the triplet state of complexesb.

Complex	E_{EM} (eV)	E_T (eV)	$\phi_T(B)$ LUMO	$\phi_T(B)$ SOMO	I_T.100
Ru(bpy)$_3$	2.07	2.30	1.00	1.00	-
C1	1.97	1.76	0.95	0.64	1.2
C2	1.87	1.54	0.94	0.43	0.4
C3	-	0.88	0.97	0.76	2.6
C4	-	1.04	0.94	0.55	1.1

With the purpose to validate the triplet state optimized geometries, triplet energies were calculated and compared with the experimental emission wavelength. Calculated values reproduce the experimental tendency. The emission energy of Ru(bpy)$_3^{2+}$ is overestimated, while it is underestimated for C1 and C2. Interestingly, predicted values for C3 and C4 are low respect to the other complexes and suggest that non-radiative decay could be a competitive process, being a possible explanation for the absence of emission in these complexes.

The fourth column of Table 2 displays values show the participation of the dicarboxibypiridine ligand in the SOMO and LUMO. As it can be appreciated, the composition of the SOMO is rather different respect to the unoccupied LUMO. This difference is most

evident for C2 and C4 complexes that exhibit low values 43% and 55%, respectively, while in the singlet state their participation is over 90%.

The available energy for injection through the triplet state (I_T) is shown in the last column. C3 shows the higher values followed by C1 and C4, while C2 is the lowest. This series of values predict a different tendency when compared to those obtained for the delivered energy (E_D) assuming hot injection; however, both results coincide, by showing that C3 is the most effective in delivering energy to anchor ligand.

As a conclusion of this study in relation to its objectives, it must be mentioned that even if the initial requirements for a good performance of a dye in a solar cell (absorption in the visible range with a high extinction coefficient) are valid, its presence does not guarantee an efficient injection process or good performance of the cell.

The composition of the absorption band must be analyzed, especially to find out the amount of electronic density concentrated on the anchoring ligand, and this factor must be thoughtfully considered in the design of new solar cell dyes.

5. The I_T Parameter: A Measure of the Electronic Density on the Anchor Group

In the previous chapter, two mechanisms for electronic transfer where proposed. In the first mechanism, the electronic injection was proposed to occur from a hot excited state in which the absorbed energy is directed towards the ligands, and where no vibrational deactivation is observed. In the second mechanism, after vibrational deactivation, the thermally balanced excited state is reached and, from there, by means of the anchor group, electronic injection towards the conduction band occurs. In this mechanism, the anchor group plays a very important role and, therefore, is central to optimize and understand its characteristics as an electronic transfer agent. Its properties of absorption on the surface of titanium dioxide are also important. From an experimental point of view, different types of chemical groups are known that can act as anchors, such as phosphonates and carboxylates, the latter being the most used for its stability.

Given the importance of the anchor group, the objective of this chapter is to analyze the performance of different types of functional groups (OH, COOH, COOEt and CN) when acting as anchors in ruthenium complexes. The study of the optical and electrochemical properties of these complexes will allow us to determine which is the most likely to act as a sensitizer for solar cells [8].

The complexes selected for this study obey the general formula $[Ru(dmbpy)_2R_2ppl]^{+2}$, where dmbpy is 4,4-dimetyl-2,2-bipyridine and R_2ppl is disubstituted pyrazino[2,3,f][1,10] phenantroline (R = CN, COOH, COOEt and OH). The general structure of these complexes is shown in Figure 13.

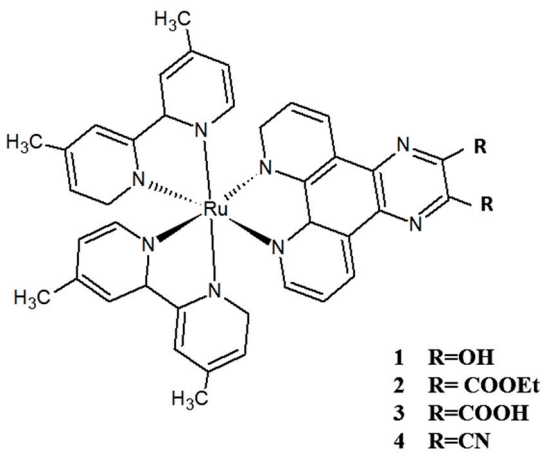

Figure 13. General structure of $[Ru(dmbpy)_2R_2ppl]^{2+}$ complexes.

5.1. Results

5.1.1. Analisys and Characterization of Ligands

The theoretical study of the ligands seeks to determine their response as electron acceptors. They can be caracterized through the electrophilicity and the charge distribution in the SOMO. For the SHE study, the ligands are visualized as decomposed into three basic fragments (B, Q, and R), as shown in Figure 14. The fragment "B" is identified with bipiridine, "Q" with the quinoxaline group, and "R" with the anchor.

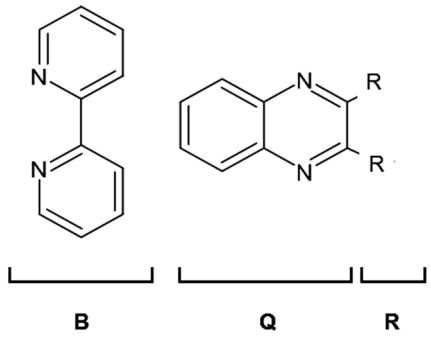

Figure 14. Decomposition of ppl-R ligands in terms of B (bipyridine), Q (quinoxaline) and R fragments.

In Figure 15, the contribution of the different fragments to the frontier orbitals is shown. The HOMO orbitals contain the B fragment, while the LUMOs are dominated by the Q fragment. In LUMO + 1, B or Q contributions are observed, depending on the substituent R.

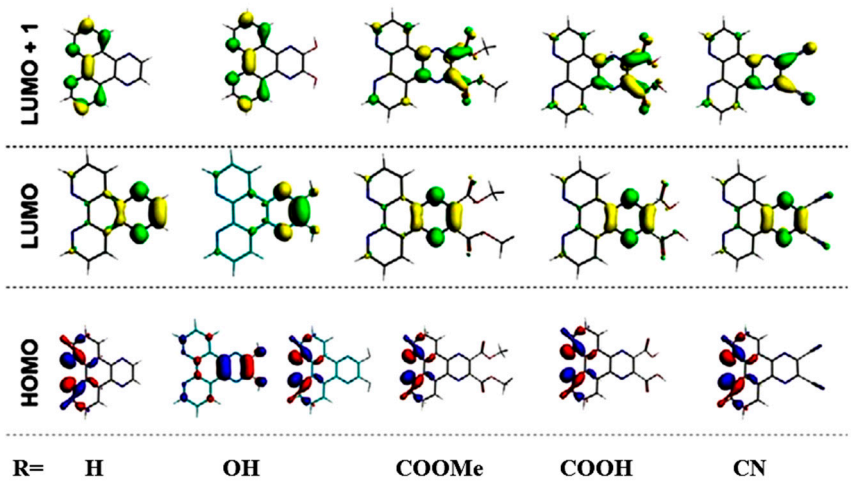

Figure 15. HOMO, LUMO and LUMO + 1 molecular orbitals of R2ppl. free ligands.

Looking for deeper information in regard to the properties of the ligands, two parameters were visualized and analyzed: electrophilicity and charge distribution.

Eletrophilicity

The influence of a substituent on the acceptor capacity of the different R_2ppl ligands is shown in Figure 16. In the left-hand side of this Figure, the electrophilicity parameter is tested in bpy type ligands, by comparing the electron acceptor capacity of the COOH group in 4,4-dicarboxy-2,2bipyridine (dcbpy) with E = 7.0, in regard to 4,4-dimethyl-2,2bipyridine (dmbpy) with E = 5.2 eV. In general, suitable R_2ppl-type ligands to be used in ruthenium complexes should display a similar electrophilicity value. According to what can be seen in Figure 16, only the R_2ppl ligands with R = COOH and CN have a similar accepting capacity.

The effect caused by R = OH is interesting since this group lowers the acceptor capacity of the ligand, which is in accordance with its electron donor behavior.

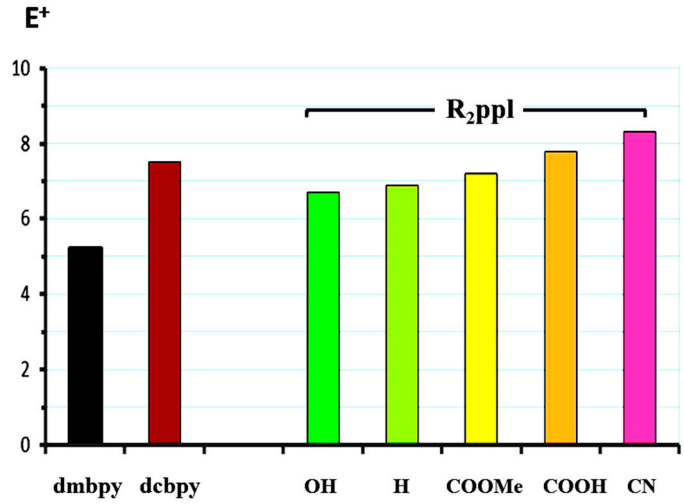

Figure 16. Electrophilicity index for R_2ppl ligands.

Charge Distribution in the SOMO

A basic characteristic for a ruthenium complex to act as a sensitizer is that it has an MLCT absorption band in the visible spectrum. This absorption band is composed ofelectronic transitions of the type d $\rightarrow \pi^*$ involving an excitation from an occupied atomic orbital of the metal to the empty LUMO of the ligand. The incoming charge is distributed throughout the different fragments that make up the SOMO orbital.

Figure 17 shows that for the reference dcbpy ligand, 29% of the incoming charge is on the carboxylated moiety (R) and 71% on bipyridine. For the ppl ligand (R = H), a different pattern is observed because an important fraction of the charge is concentrated in the Q fragment and not in R. The participation of the anchor group increases according to the acceptor capacity of the anchor. The behavior is different when R = OH since most of the charge tends to concentrate in the B (bipyridine) fragment.

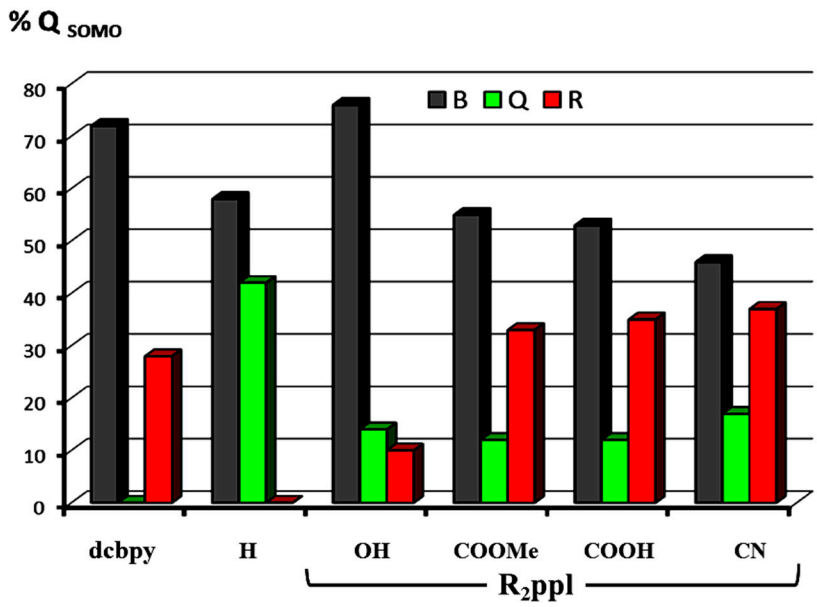

Figure 17. Charge distribution on B, Q, R fragments in the SOMO orbital.

5.1.2. Analisys of Complexes

In Table 3, the optical and electrochemical values obtained for the set of complexes under study are summarized. The acceptor behavior of the unsubstituted ppl model ligand can be observed when comparing complex 6 with 5: the presence of a ppl ligand, instead of a dmbpy ligand, causes an increase in oxidation potential from 1.09 V to 1.24 V. Electron withdrawing groups R on R_2-ppl reduce the electronic density in the ruthenium atom and, consequently, the oxidation potential continues to increase. The reduction process is more sensitive to this effect, decreasing $E_{1/2}$. In all cases, the first and second reduction processes were assigned to the R_2ppl acceptor ligand. In complex **2**, the third process was assigned to the dmbpy ligand. In complex **1**, the reduction process is irreversible; therefore, it is not possible to compare it with the other complexes.

Table 3. Electrochemical and UV–Vis absorption properties of $[Ru(dmbpy)_2R_2ppl]$ complexes in acetonitrile.

Complexes		Oxidation $E_{1/2}$/V	Reduction $E_{1/2}$/V	Absorption λ_{max}/nm	Assignment
$[Ru(dmbpy)_2\ ppl(OH)_2]^{2+}$	**(1)**	1.22	−0.95, −1.11	**457**	MLCT
$[Ru(dmbpy)_2\ ppl(COOEt)_2]^{2+}$	**(2)**	1.28	−0.89, −1.19, −1.47	**442**	MLCT
$[Ru(dmbpy)_2\ ppl(COOH)_2]^{2+}$	**(3)**	1.29	−0.87	**450**	MLCT
$[Ru(dmbpy)_2\ ppl(CN)_2]^{2+}$	**(4)**	1.39	−0.86	**446**	MLCT
$[Ru(dmbpy)_2\ ppl]^{2+}$	**(5)**	1.24	−1.23	**450**	MLCT
$[Ru(dmbpy)_3]^{2+}$	**(6)**	1.09	−1.47	**560**	MLCT

The effect of the anchor group on the maximum absorption of the MLCT band of the complexes can be evidenced by taking the value of complex 5 with R = H and λ_{max} = 450 nm as a reference. The presence of the COOEt and CN groups causes an hypsochromic shift in the maximum of the band to 442 and 446 nm, respectively, while when R = OH, the maximum undergoes a bathochromic shift towards 457 nm.

These results show that the anchor group can influence the absorption spectrum through its donor or acceptor capacity. In other words, what is being observed is that there is a connection between the absorption spectrum and the anchor group, so that part of the absorbed energy is directed towards it. This is especially true for complexes with R = COOMe, COOH and CN.

Molecular Orbitals

The diagram in Figure 18 shows the energy levels and the composition of HOMO and LUMO for the entire series of complexes. The HOMO orbital of these compounds is composed mainly of metal atom orbitals, and only a small contribution from ligands (3%) is observed. The energy of this orbital has the meaning of an ionization potential and, therefore, linearly correlates (0.98) with the oxidation potential, as shown in Figure 19a. The influence of electron donor substituents causes a progressive stabilization of energy which is reflected in an increase in the oxidation potential.

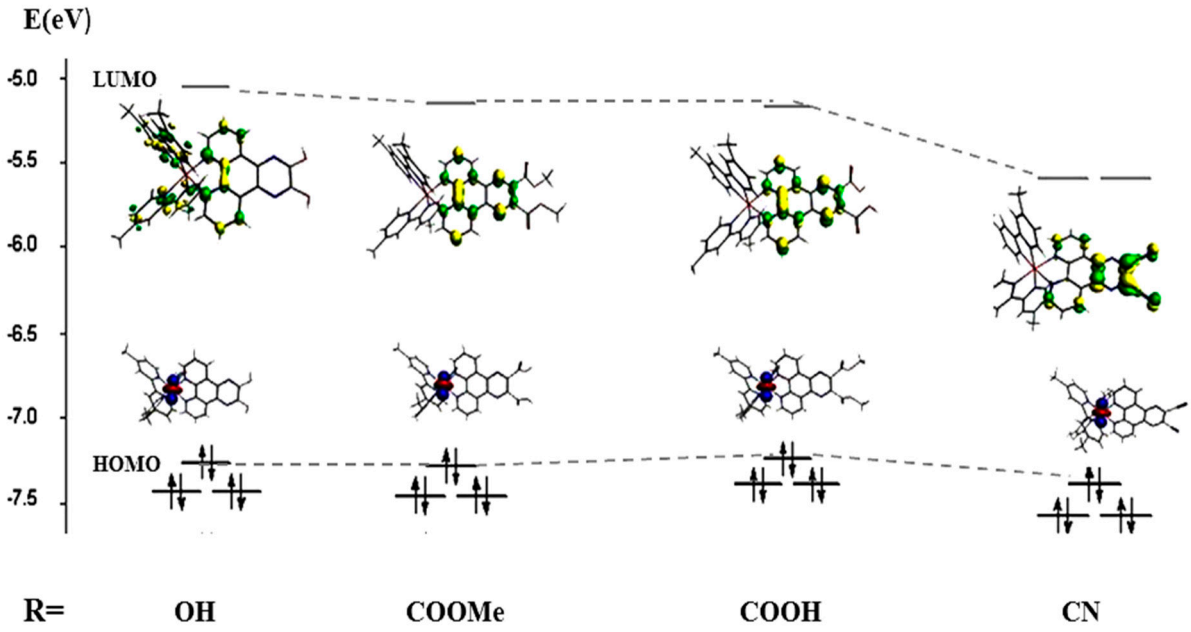

Figure 18. Molecular orbital scheme for $[Ru(dmbpy)_2R_2ppl]^{2+}$ complexes.

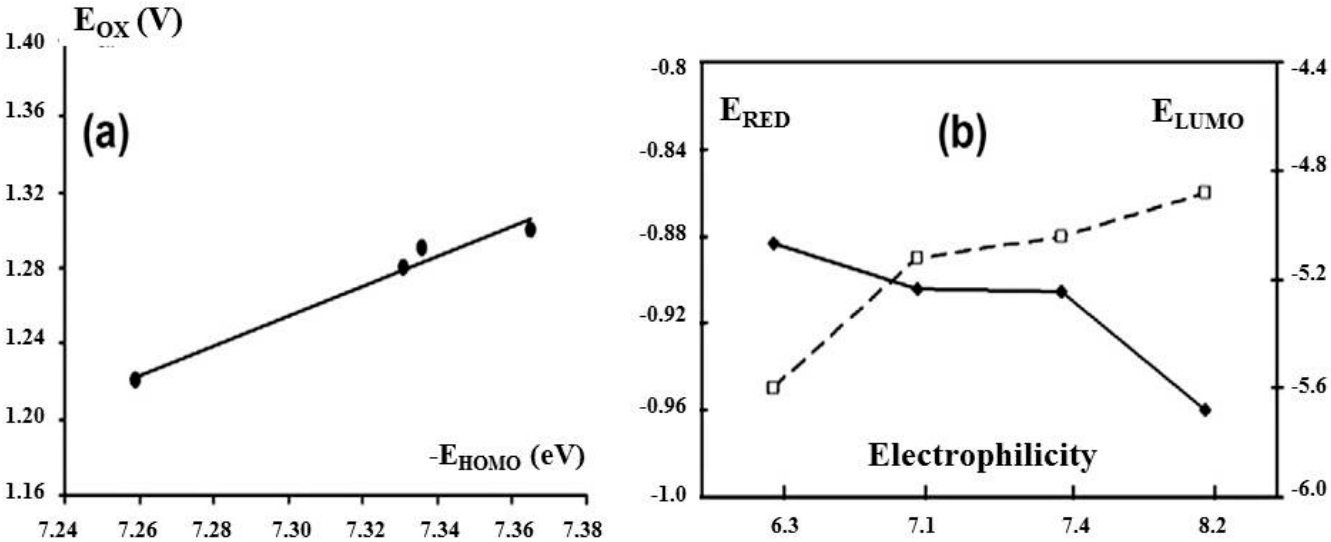

Figure 19. (**a**) Linear correlation between the oxidation potential and the HOMO energy. (**b**) Influence of the ligand electrophilicity on the reduction potential (line) and in the LUMO energy (dash).

The LUMO orbital is centered on the R_2ppl ligand and its composition is a mixture of the B, Q and R fragments; the predominance of one or the other depends on the nature of the R component. For example, the electron donor substituent R = OH localizes electronic density in the bipyridine ring of ppl, while electron-acceptor substituents such as CN and COOH involve the participation of the QR fragments.

Figure 19b reveals an interesting relationship between the reduction potential, the energy of the LUMO and the electrophilicity of the anchor ligand: when the electrophilicity increases from 6 eV to 8 eV, the LUMO stabilizes (from −5.1 eV to −5.7 eV) and the reduction potential diminishes from −0.95 V (R = OH) to −0.86 V (R = CN).

Evaluation of Complexes as Dye Sensitizers

The evaluation of the ruthenium complexes as suitable candidates for a DSSC could be achieved by calculating a theoretical index using equations previously derived in Section 3.2.

For this purpose, the model that involves the participation of the anchor group in the triplet state throughout the parameter. It was chosen instead of the hot injection possibility (Section 3.1) where the absorbed energy was transmitted through the anchor ligand in a hot vibrational state.

Figure 20 shows a basic description of how the different groups composing the ruthenium dye act in order to transfer the sunlight absorbed energy to the conduction band of the semiconductor. As mentioned before, in the present model it is assumed that the anchor ligand acts as a donating group, and that the charge concentrated in this anchor group is the charge available to be injected to the semiconductor.

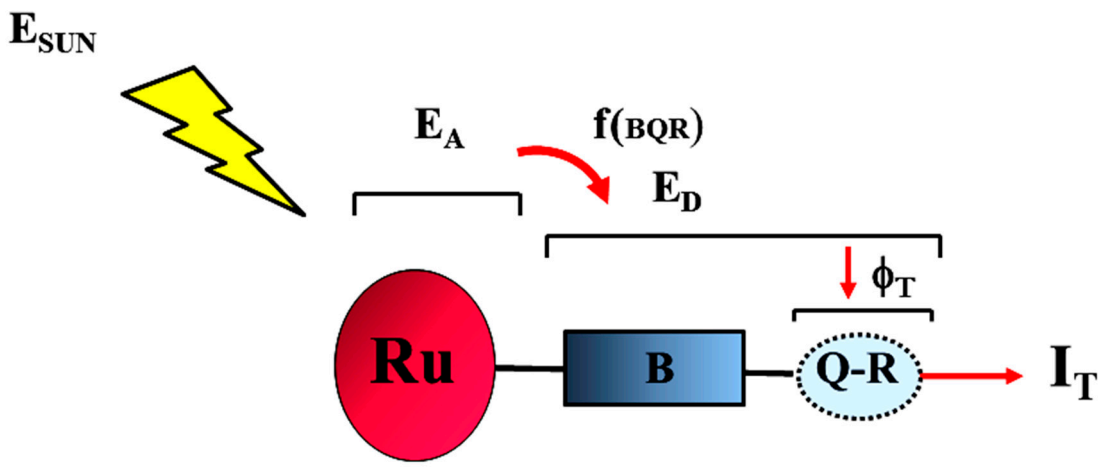

Figure 20. Description of the energy flow on a ruthenium complex containing an anchor ligand composed by BQR fragments.

The amount of energy (I_T) that can be delivered to TiO_2 from the acceptor anchoring ligand (R_2ppl) through the anchor group (R) in the electronic thermally equilibrated, thexi, state T_1, is calculated from Equation (22),

$$I_T = E_D \phi_T(QR) \tag{22}$$

where ϕ_T is the intersystem crossing constant obtained from the composition of the SOMO on the triplet state configuration. E_D is the delivered energy,

$$E_D = E_A f(BQR) \tag{23}$$

that depends on the amount of absorbed energy, E_A, that is deliverd to the anchor ligand.

$$E_A = \sum_{\lambda} f_\lambda E_\lambda \tag{24}$$

In the case of the hot injection mechanism, the crosslinking of systems does not occur, and all the absorbed energy is delivered to the anchor ligand and is available (I_S) to be injected through the singlet state.

$$I_S = E_D \text{ when } \phi_T = 0 \tag{25}$$

Employing this set of equations with data provided by TDDFT, it becomes possible to determine the amount of energy from the sunlight spectra absorbed by the complex (E_A), which reaches the anchor ligand (E_D) from the triplet state (ϕ_T), and that is available to be injected (I_T).

In summary, the main objective of this chapter was to develop the theoretical I_T index that allows us to calculate the amount of energy absorbed from sunlight that is available to be injected. The values obtained through the calculations are shown in Table 4. For the

purposes of comparative analysis, the It value for complex 5 is taken as a reference. The table shows that complex 5 absorbs 1.87 eV, delivering part of it, 0.77 eV, to the anchor ligand, where it concentrates on the anchor group with an efficiency of 83%. With all this information, the It parameter, representing the energy available to be injected, can be calculated, corresponding to 0.64 eV. The presence of ppl(COOH)$_2$ instead of dcbpy, complex 3, generates a complex with similar absorbed energy, 1.89 eV, but the delivered energy drops to 0.44 eV and only 31% is received by the anchor group. The value of It = 0.14 clearly indicates that there is a great difference between both ligands in terms of transmitting the absorbed energy. Within the R$_2$ppl series, complexes with R = COOMe and R = CN possess lower It values than the carboxy substituent.

Table 4. Calculated values of I_T for R$_2$ppl complexes.

Complexes		E_A	E_D	φ_T	I_T
[Ru(dmbpy)$_2$ ppl(OH)$_2$]$^{2+}$	**(1)**	1.31	0.39	0	0
[Ru(dmbpy)$_2$ ppl(COOEt)$_2$]$^{2+}$	**(2)**	1.12	0.33	0.30	0.1
[Ru(dmbpy)$_2$ ppl(COOH)$_2$]$^{2+}$	**(3)**	1.89	0.44	0.31	0.14
[Ru(dmbpy)$_2$ ppl(CN)$_2$]$^{2+}$	**(4)**	1.10	0.23	0.52	0.12
[Ru(bpy)$_2$ dcbpy]$^{2+}$	**(5)**	1.87	0.77	0.83	0.64

The low efficiency values presented by these complexes can be attributed to two causes: (1) the different fragment composition of the ppl(COOH)$_2$ respect the dcbpy ligand, reduces the amount of delivered energy to the anchor group, and (2) the participation of the anchor group on the thexi state is greater in the dcbpy than in the ppl ligand.

If we compare these results with those obtained by the hot injection mechanism where no intersystem crossing occurs, and therefore all the available energy for injection (I_S) is the delivered energy (E_D), complex 3 displays the higher value followed by the ester substituted and the cyanide group. This tendency is different to that predicted from the thexi state were the cyanide group exhibit a higher value that the ester substituent.

In conclusion, although the types of ligands chosen for this part of the study are not very promising for dye use in solar cells, the method developed in this chapter allowed us to calculate a theoretical index that measures the amount of energy available to be injected. This index can be related to light harvesting efficiency, one of the three parameters composing the experimental PCE.

The other two factors, electronic injection and regeneration, cannot be calculated by means of this model since it is established that the load reaches only the anchor group. To include and calculate the other two factors, it is necessary to build a new system of the type donor–linker–acceptor (DolAc), where the complex is attached to some acceptor that simulates the behavior of titanium dioxide. This will be worked out in the next chapters.

6. Reproducing the Photo Conversion Efficiency of a series of Ruthenium Dyes with a Three-Parameter Model

The BCL approach [18] merged as a theoretical tool to help to understand the results obtained for the efficiency of five ruthenium dyes measured in the same experimental conditions. The set of ruthenium complexes was chosen according to a predefined strategy, that consisted in modifying physical properties of the [Ru(dcbpy)$_2$]$^{+2}$ core by incorporating different types of ligands, and then observing how these changes influenced the overall performance of the solar cell. Figure 21 displays the different types of ligands that were employed: bipirydine, thiocianate, phenylpirydine and 4,4´distyril,2,2´dipyridine (LH). The general design follows according to the following sequence: starting with the unsubstituted complex, C1, a thiocyanate ligand was introduced giving the N3 complex labeled as C2. When SCN is replaced with the cyclometalated ligand the C3 complex is obtained.

Changing one bpy of C1 with one LH chromophoric ligand gives C4 and introduces a second chromophore result in complex C6.

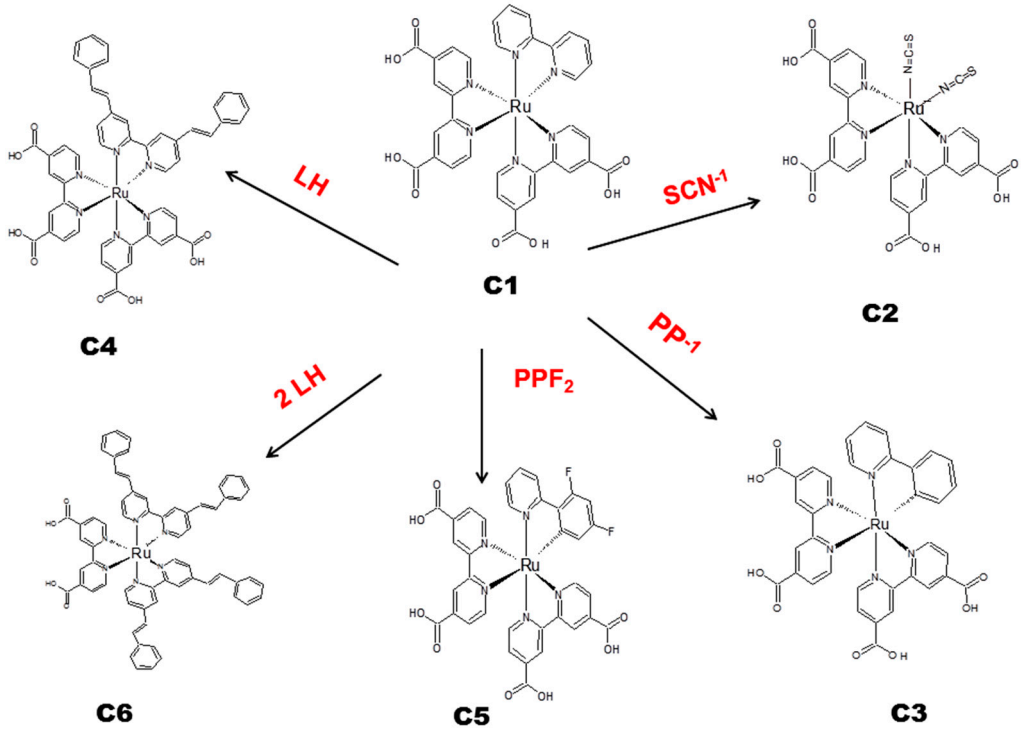

Figure 21. Complexes employed in this study. C1 is the base complex, and the effect on the cell efficiency of replacing the 2,2′-bpy ligand by: SCN^- (C2), PP^{-1} (C3), LH (C4), PPF_2 (C5) and two LH gives (C6).

Figure 22 shows the induced photocurrent efficiency measured for the five complexes. Some general conclusions can be obtained. For example, C2 displays a far better response than the other dyes, until 600 nm, where it begins to decay. A detailed comparison between the other dyes seems difficult since their relative response varies along wavelength. A complementary analysis can be done by looking for wavelength independency in the 400–600 nm range. This is achieved by dividing the IPCE by the absorptance, obtaining the absorbed photocurrent efficiency (APCE) (Figure 22b).

The independent behavior of the APCE in regard to wavelength was identical all five dyes, reflecting the independence of the APCE toward the excitation energy. This is compatible with a mechanism were the electron injection proceeds through only one excited state. This mechanism differs from the previous reported for the N3 dyes, where electron injection was attributed to a set of hot excited states.

Finally, it can be stated that the type of ligand exerts an influence on the overall efficiency according to C2 >> C1> C6 > C3 > C4.

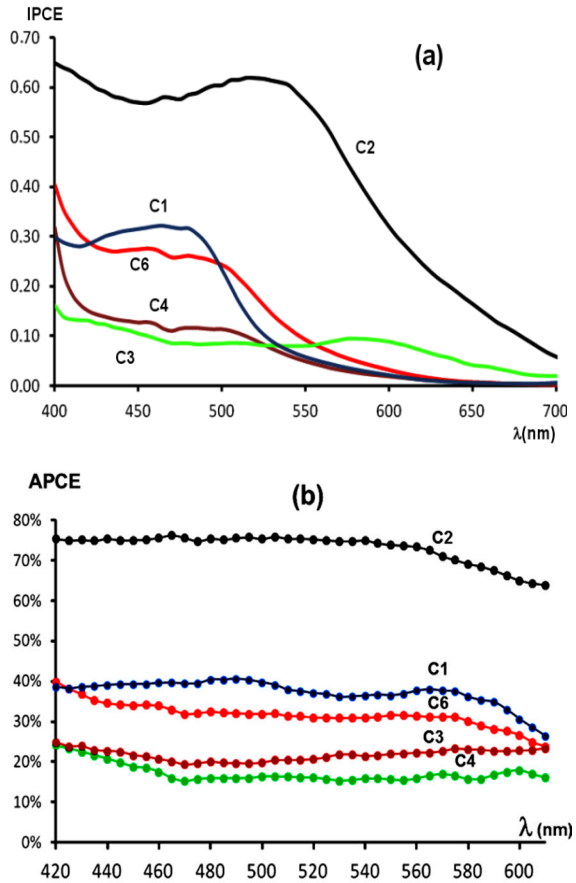

Figure 22. (**a**) IPCE (**b**) APCE for the series of complexes under study.

6.1. Theoretical Background

6.1.1. The Global Efficiency Index

To understand these results, we proposed building a theoretical index (GEF), the Global Efficiency Index, calculated by employing data obtained from computational simulations of the ruthenium dyes anchored to the titanium dioxide surface. In this sense, a DSSC can be de described as part of a general class of donor–linker–acceptor (DolAc) systems, where an electron transfer process occurs from a donor to an acceptor via an organic linker. In the present model, the donor is ruthenium complex, the acceptor is a $[Ti(OH)_3]^+$ unit and the linker is a the carboxilate moiety.

In the previous work, the donor group was located on the ruthenium complex, while the acceptor was centered on the anchor ligand. Through this model, a general set of equations was derived to calculate how much of the absorbed energy by the dye could reach the anchor ligand and be available for injection.

The model went further, by now considering the ruthenium complex (D) bound to a model of the semiconductor, a $Ti(OH)_3$ group, forming a stable adduct labeled, $[D\text{-}Ti(OH)_3]$. In this way, the charge of the carboxilated group is neutralizated by a $Ti(OH)_3{}^+$ unit, both constituting the transferring center to inject electronic density to the semiconductor. In the DolAc architecture, the acceptor and donor groups are linked by the carboxilate moiety, and charge will flow from the SOMO of the excited ruthenium dye to the LUMO of $Ti(OH)_3$.

The Global Efficiency Index (GEI) is calculated as the product of three independent parameters, **GEI = $F_1F_2F_3$**, that take into account the efficiency of the main three chemical process governing the operational cycle of the DSSC.

$D\text{-}Ti(OH)_3- + h\upsilon \rightarrow D^*\text{-}Ti(OH)_3$ (F1);
$D^*\text{-}Ti(OH)_3 \rightarrow D^+\text{-}Ti(OH)_3(-)$ (F2);
$D^+\text{-}Ti(OH)_3 + R^- \rightarrow D^+\text{-}Ti(OH)_3 + R$ (F3).

The three processes labeled F1, F2, and F3 are related to three fundamental processes governing the efficiency of a sensitized solar cell: the harvested energy (F1), the injected energy (F2) and the regeneration efficiency (F3).

In the following, a description of the F1, F2, and F3 parameters is presented.

6.1.2. Available Energy for Injection (F1)

The F1 parameter showed on Figure 23 is obtained by calculating the available energy through the I_T parameter previously defined by a set of equations that enable the calculation of the absorbed energy (E_A), the delivered energy (E_D) on the anchor ligand (LAn), and the available energy for injection (F1):

$$E_A = \sum_{\nu} E_\nu f_{osc} \tag{26}$$

$$E_D = E_A f(LAn) \tag{27}$$

$$\text{F1} = E_D \phi_T(An) \tag{28}$$

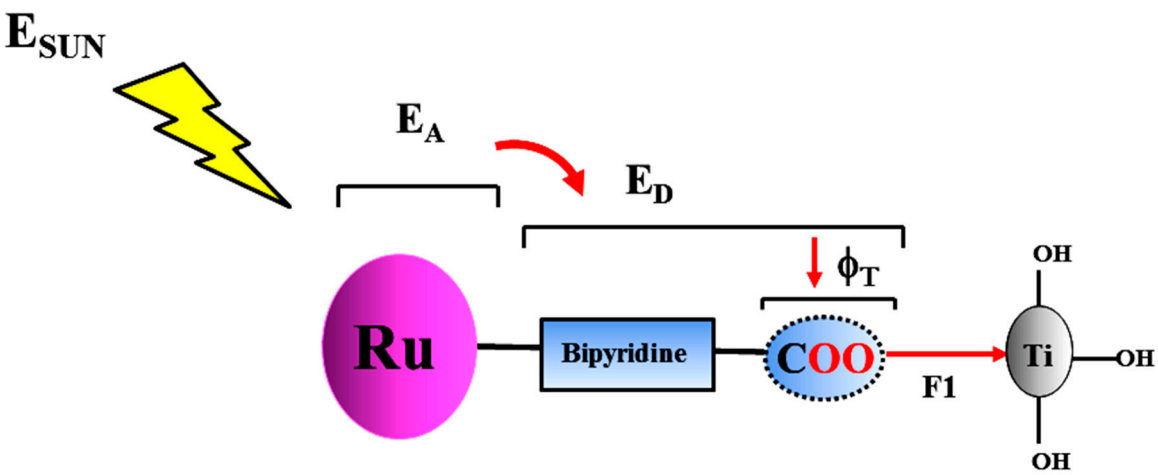

Figure 23. Scheme showing the composition of the F1 index.

These parameters are determined with data obtained from TDDFT calculations that provide the energy and the oscillator strength at which an excitation occurs, the distribution function value for the anchor ligand, $f(LAn)$, and the participation of the anchor group on the triplet state, $\phi_T(An)$.

6.1.3. Amount of Charge Injected (F2)

The Linker–Acceptor Interface

The second index represents the amount of charge injected and is calculated employing an electrostatic model for modeling the linker–acceptor interface. After geometrical optimization of the triplet state of the complexes bounded to $Ti(OH)_3$, the atomic distances and Mulliken's charges displayed on Figure 24 were calculated. The values of both parameters remain the same for all the series, therefore appearing not to be influenced by the type of ligand.

The carboxylate moiety contains two different interatomic distances between C and O, in accordance with a ketonic (1.25 Å) and ether (1.31 Å) types of bonding. As expected, the electron transfer process occurs between the acceptor and the donor. In this case, the donor is located on the moiety formed by the titanium atom with a positive charge, surrounded by four negative-charge oxygen atoms. The donor site is located in O_1 which is at 2.00 Å from the acceptor. Its donor capacity is influenced by the net electrostatic potential created

by the charge distribution composed by the two positive charges on Ti and C1 and the negative charge on O_2.

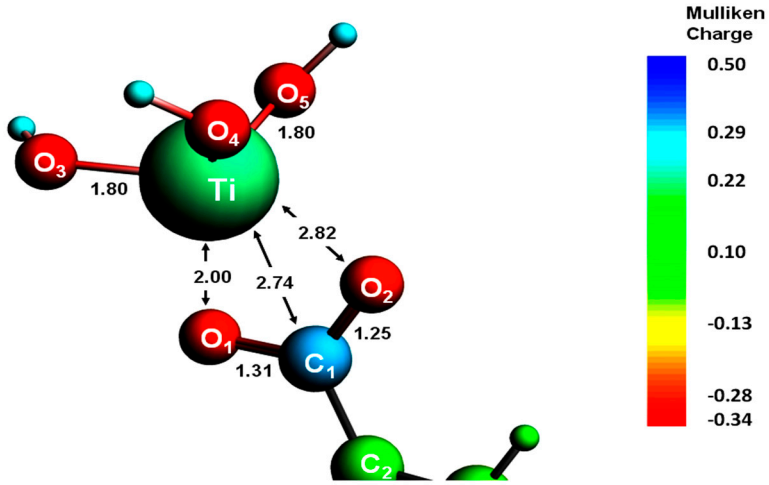

Figure 24. Inter-atomic distances and Mulliken's charge analysis on the [R-COO-Ti(OH)$_3$] interface.

Electron Injection

The electronic transfer mechanism proposed contains three stages as shown in the upper part of Figure 25. The DLan-Ti(OH)$_3$ adduct is excited in the first step (a) resulting in a charge separation state, step (b), where an electron populates the SOMO level of the dye. Finally, in step (c), the electron migrates to the LUMO of the Ti(OH)$_3$ unit.

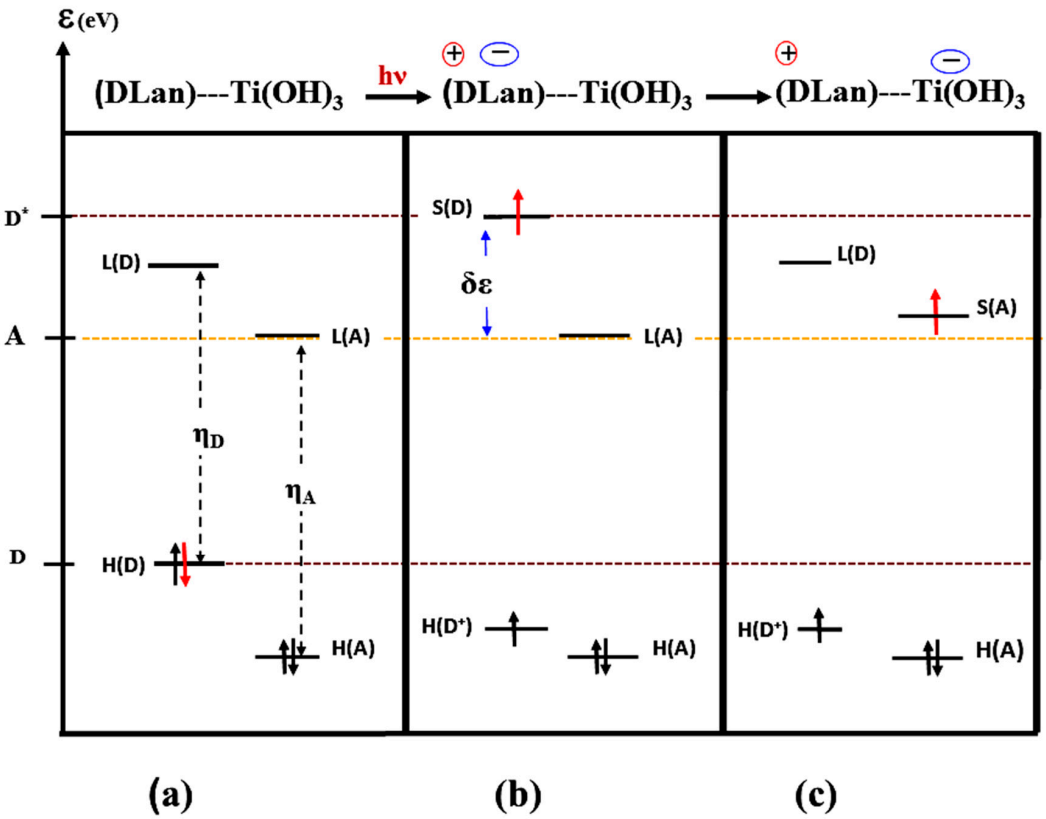

Figure 25. Molecular orbitals involved in the electron injection: (**a**) Ground state; (**b**) thexi state; (**c**) charge separate state. H(D) = HOMO of the Donor, L(D) = LUMO of the Donor S(D) = SOMO of the Donor, η_D, η_A = Hardness of Donor and Acceptor.

At the bottom of Figure 25, the molecular orbitals involved in this process are displayed. In step (b), an energy gradient ($\delta\varepsilon$) is created product of the difference between the chemical potential of the SOMO (μ_D^0) and the LUMO (μ_A^0) of the acceptor. This difference is minimized when an amount of electronic charge (δq) is transferred when both potentials equalize $\mu_A = \mu_D$.

$$\mu_D = \mu_D^0 + 2\eta_D\,\delta\mathrm{q} + \mathrm{V_{el1}} \tag{29}$$

$$\mu_A = \mu_A^0 + 2\eta_A\,\delta\mathrm{q} + \mathrm{V_{el2}} \tag{30}$$

$$\delta\mathrm{q} = \frac{\mu_D^0 - \mu_A^0 + V_{el12}}{2(\eta_D + \eta_A)} \tag{31}$$

In Equation (30), the δq value can be identified with the F2 index when suitable values are employed to evaluate it. In this sense, $\mu_D^0 = \varepsilon_{SOMO}$ and $\mu_A^0 = \varepsilon_{LUMO}$ can be employed. On the other hand, the electrostatic potential term is calculated as $\mathrm{V_{el1}} = \sum_{\mathrm{i}} \frac{\mathrm{q_i}}{\mathrm{r_{iA}}}$ from the charge distribution and the global hardness through the difference $\varepsilon_{LUMO} - \varepsilon_{HOMO}$.

$$\mathrm{F2} = \frac{\varepsilon_{SOMO}(D) - \varepsilon_{LUMO}(\mathrm{Ti(OH)_3}) + \mathrm{V_{el12}}}{2\left(\eta_D + \eta_{\mathrm{Ti(OH)_3}}\right)} \tag{32}$$

It is interesting to note that for the case in which the performance of several types of donors in contact with a single acceptor is studied, two terms of Equation (31) remain constant, $\mathrm{V_{el12}}$ and $\eta_{\mathrm{Ti(OH)_3}}$, whereby this equation can approximate and give origin to:

$$\mathrm{F2} \approx \frac{\delta\varepsilon}{2\eta_D} \tag{33}$$

Equation (33) provides a very interesting and unexpected result. It follows that the amount of charge injected depends on the energy difference between the SOMO of the excited dye and the LUMO of the acceptor group. Consequently, as the difference increases, the injection should also increase. However, Equation (33) states that this not to occur, because $\delta\varepsilon$ is modulated by the hardness of the dye: $\varepsilon_{HOMO} - \varepsilon_{LUMO}$.

Accordingly, dyes with low hardness (soft) will increase F2, while complexes with high hardness will diminish it. In this sense, soft complexes with a low band gap energy and high polarizability will be highly suitable to increase the electronic injection.

6.1.4. Effectivness of Regeneration (F3)

The third parameter is the $\mathrm{F_3}$ index, which is designed to measure the effectiveness of the regeneration of the oxidized dye by the redox mediator couple ($R^-/\mathrm{R^0}$) added to the solvent. The regeneration process is represented as an equilibrium between two competing species:

$$\left[\mathrm{D^+}\right] - \mathrm{Ti(OH)_3} + R^- \rightleftarrows \left[\mathrm{D}\right] - \mathrm{Ti(OH)_3} + \mathrm{R^0} \tag{34}$$

For an efficient regeneration process, it is necessary that Equation (34) is displaced to the right, $\mathrm{K_{eq}} > 1$. Considering the Nernst equation, an exponential relationship existing between the equilibrium constant and the free energy change is observed. This can be related to the difference between standard redox potentials, $\Delta E = \varepsilon_{ox}^0(R^-) - \varepsilon_{red}^0(\mathrm{D^+})$. In this way, $\mathrm{F_3}$ is a measure of the amount of displacement to the right of Equation (34), and is expressed as

$$\mathrm{F_3} = \alpha \mathrm{e}^{-\Delta\varepsilon} \tag{35}$$

where α is a proportionality constant and $\Delta\varepsilon$ as the difference between the ionization potential of R^- and the electron affinity of $\mathrm{Ru^{+3}}$ oxidized dye, which is roughly the negative of the ionization potential of $\mathrm{Ru^{+2}}$.

$$\Delta\varepsilon = \varepsilon_{HOMO}(R^-) - \varepsilon_{HOMO}\left[\left(Ru^{+2}\right) - \mathrm{Ti(OH)_3}\right] \tag{36}$$

As $\Delta\varepsilon$ increases, the equilibrium constant also increases, and Equation (34) is displaced to the right favoring the regeneration of the dye and the beginning of a new photo catalytic cycle. Figure 26 compares the ionization potential of Iodide, di-Iodide and tri-Iodide species, commonly employed as regenerators for DSSC, with the calculated electron affinity for the set of ruthenium dyes.

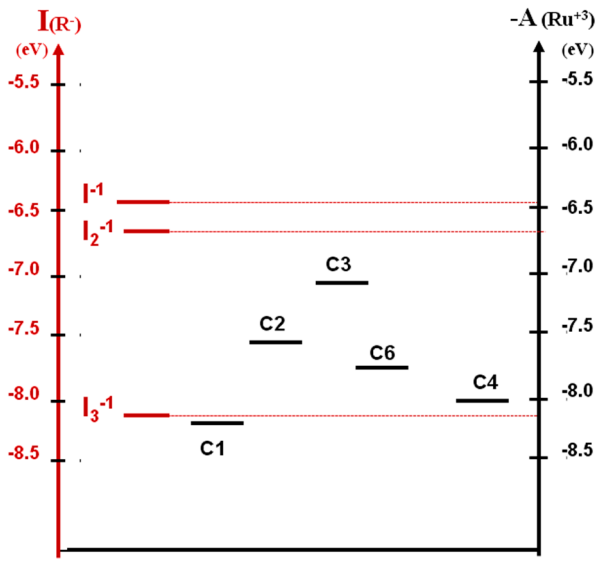

Figure 26. Ionization potential for iodide species, and electron affinity for ruthenium complexes.

The results show that iodide and di iodide present a low value of the oxidation potential, which allows us to reduce, and consequently regenerate, the entire series of complexes from C1 to C6. On the other hand, C3, the cyclometalated complex, has the higher electro affinity and, therefore, is the most difficult to reduce, while C1 would be the easiest. This last complex has the particularity that it can also be reduced by the triiodide when it is present in the electrolyte.

6.2. Results

6.2.1. Aceptor–Donor Properties of a Ligand

In the above analysis, and in accordance with Equation (33), one the factors that could increase the electron injection is related to the softness and polarizability of the anchor ligand. Keeping this objective in mind, a suitable characterization of the ligands in order to determine their acceptor/donor character should be helpful to understand how they influence the performance of the DSSC. The forthcoming classification is based in three theoretical parameters: orbital hardness (η^+), polarizability (α_0), and electrophilicity (E).

The first index is a measure of the resistance to deliver charge, the second is the deformation of the electronic cloud in presence of an electric field, and finally, the third is a measure of the power of the stored electronic charge. The results of this study are relevant for the design of new ligands for complexes supporting a DolAc architecture.

Figure 27 displays the six types of ligands incorporated in this study, which are currently employed in DSSC devices. They are ordered according to their decreasing orbital hardness. This theoretical index measures the resistance of the SOMO orbital to deliver electronic charge. Ligands with high orbital hardness are good donors and are hard in the sense of Pearsons's acid–base theory.

Accordingly, thiocianate is the hardest ligand and is followed by phenyl pyridine. Softness is measured in terms of the calculated average polarizability and shows that carboxylate groups and highly delocalized ligands increase the polarizability and become good acceptors according to the Electrophilicity index.

The acceptor capacity is related to the ability of the SOMO to distribute electronic charge along the carbon skeleton. Dcbpy and tctpy belong to this category. On the other side, thiocyanate, because of its low polarizability and null electrophilicity, is a good donor.

LIGAND	NAME	Hardness η^+ (eV)	Polarizability α (ua)	Electrophilicity E (ua)	SOMO
SCN	SCN	7.6	32	0.1	
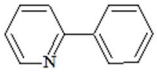	pp	6.9	148	4.0	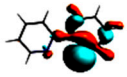
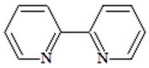	bpy	4.8	129	10.8	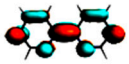
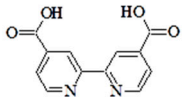	dcbpy	4.1	170	14.8	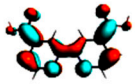
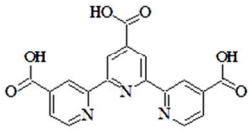	tctpy	3.4	266	15.5	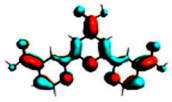
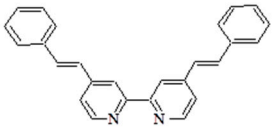	LH	3.1	400	14.3	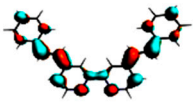

$\eta^+ = \delta\varepsilon_F/\delta n_F$, $\bar{\alpha} = \frac{1}{3}(\alpha_X + \alpha_Y + \alpha_Z)$,$E=\mu^2/2\eta$

Figure 27. Comparison of calculated properties for different types of Ligands.

6.2.2. Theoretical Evaluation of Complexes as Sensitizers

The idea behind this theoretical evaluation is to obtain a reliable parameter from ab initio calculations that could be employed to compare the suitability of different type of ruthenium complexes to act as sensitizers.

The global efficiency index is built as the product of three independent parameters, which means that an increase in the value of one of them is not necessarily reflected in the other two. Accordingly, a champion dye is the result of a collaborative relationship between the three independent indexes which is reflected on the final whole value.

Table 5 summarizes the values obtained for six different ruthenium dyes. The % of Global Efficiency Index is obtained by dividing the product $F_1F_2F_3$ by Esun (4.18 ev) which is the maximum energy emitted in the range of 400–700 nm.

Table 5. Calculated values for the Global Efficiency Index (GEI) has the product of F1, F2, and F3 parameters.

COMPLEX	EA	ED	Φ_t	F1	$\Delta\varepsilon$	ΔV_{DA}	F2	F3	%GEI
C1	0.92	0.38	0.06	**0.02**	1.03	−0.26	**0.09**	**5.87**	**0.27**
C2 (N3)	0.91	0.59	0.12	**0.07**	1.26	−0.31	**0.12**	**3.06**	**0.64**
C3	0.93	0.28	0.11	**0.03**	1.54	−0.31	**0.16**	**1.99**	**0.23**
C4	1.57	0.35	0.03	**0.01**	1.21	−0.26	**0.11**	**4.66**	**0.13**
C6	3.74	0.42	0.07	**0.03**	1.32	−0.28	**0.12**	**3.77**	**0.33**
C5 (ppf2)	1.58	0.45	0.10	**0.05**	1.33	−0.30	**0.13**	**2.77**	**0.44**
BD	1.06	0.96	0.15	**0.15**	1.11	−0.32	**0.11**	**3.13**	**1.25**

In Table 5, the calculated values obtained for the three factors F1, F2, and F3 are displayed along with their components: EA, ED, and Φt for F1, and the sum of the global hardness, Δε, and ΔV for F2. The last column of the table shows the Global Efficiency Index (GEI) obtained as the product of the three indexes, F1, F2, and F3. According to this index, the C2 complex displays the higher value followed by C6 and C1. The complex with one chromophoric ligand is the worst. The reason why C2 is successful lies in the higher value of F1: it possesses the higher efficiency for collecting and delivering energy to the anchor group (F1 = 0.07). The other two indexes do not show great difference with the other complexes.

On the other hand, the cyclometalated complex is very inefficient for delivering energy (F1 = 0.03); however, it possesses the higher value for injecting energy (F2 = 0.16) due to the high value of the SOMO, but a very low efficiency of regeneration with iodide (F3 = 1.99). Figure 28 displays the values of the GEI in decreasing order for the four complexes which follow the same trend observed for the APCE.

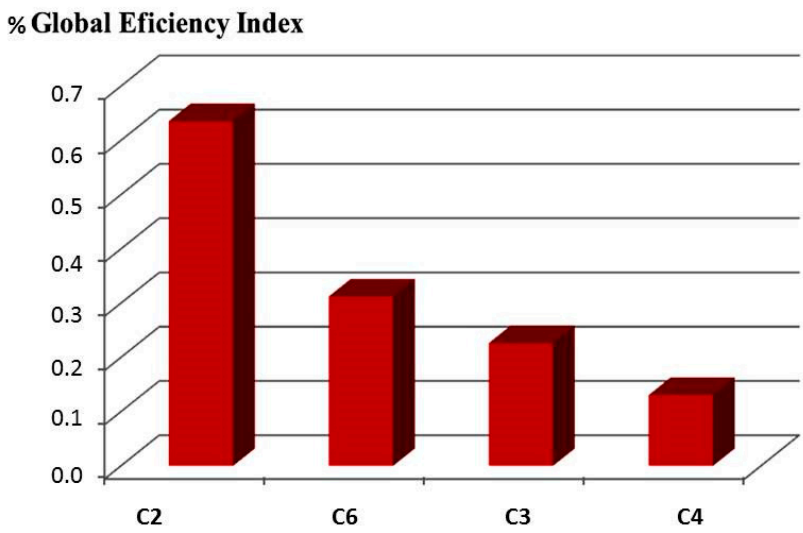

Figure 28. Comparison of calculated values of GEI for C2, C3, C4 and C6.

The previous comparison of calculated GEI values with APCE reveals and important correlation between them; however, it is more suitable to compare it with the Photo Conversion Efficiency (PCE) index, a parameter that measure the efficiency of a DSSC under standard condition of irradiance, air mass, and temperature. The reported values found in the literature of four different ruthenium dyes are compared with calculated GEI. The series start the reference complex C1, followed by the C5 complex which is the fluorinated version of C3. The two other dyes shown belong to the category of champion dyes and are the N3 dye and the back dye (BD), where the dcbpy is replaced by the tricarboxylated terpyridine(tcpy) ligand.

From Figure 29, it can be concluded that the GEI correctly reproduces the increasing tendency of the PCE for these complexes and establishes that the BD is the most efficient among them. These results can be understood by inspecting the data from Table 2. For the case of C5, it is clear that the two Fluor on the phenyl ring cause a positive impact and boost the F1 and F3 indices with respect to C3. The stabilization of the SOMO level causes a lowering of the band gap energy (1.54 vs. 1.33) and diminishes the amount of energy injected through F2. However, this reduction is compensated by the increase in F1 and F3 and push up the global giving rise to the increase in GEI from 0.23 to 0.40.

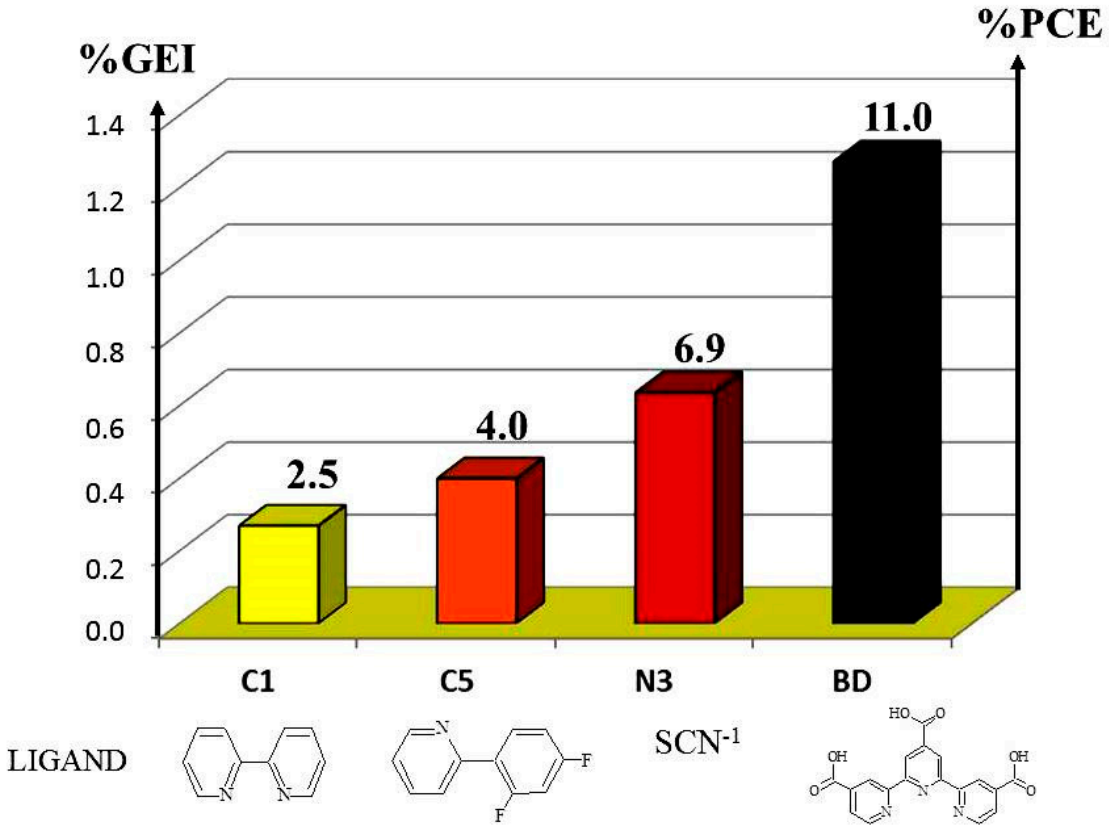

Figure 29. Correlation between GEI and PCE.

The BD complex possesses the higher value of GEI, coincident with the maximum photo conversion efficiency observed among this series of ruthenium dyes. According to the model herein described, the good match observed between the experimental PCE values and the theoretically predicted efficiency is attributed partly to the soft properties of this ligand, and to the high rate for delivering energy to the anchor group (F1 = 0.15). Interestingly, the absorbed energy by the BD is 1.05 eV very close to the values of N3 (EA = 0.92) and C1 (EA = 0.91).

However, the delivered energy is rather different ED = 0.93 compared with 0.58 of N3 and 0.38 of C1. It is also possible to highlight the greater participation of the anchor group in the thexi state Φ_t = 0.15 that is twice the value of N3.

Concluding, the global efficiency index GEI obtained through the BCL model including the product of three factors, permitted to reproduce the experimental photo conversion efficiency tendency for a series of complexes. This new index contains important information to be used in the development of new solar cells.

7. The Role of Lithium on the Photo Conversion Efficiency of Ruthenium Dyes

A few decades ago, researchers showed that the presence of lithium in the electrolyte enhances the performance of the cell [19]. This effect was attributed to the intercalation of the atom in the surface of titanium dioxide, which lowers the semiconductor energy band gap. On the other hand, the interaction of the lithium cation with ruthenium complexes containing dicarboxibipiridine ligands has been used as evidence in a series of studies employing different spectroscopic techniques. It has been confirmed [20] that the presence of the cation causes a red shift of the MLCT absorption band, a quenching of the fluorescence and the increase in the Ru(II)/Ru(III) oxidation potential.

Another series of studies employing photoinduced and transient absorption spectroscopy on ruthenium dyes anchored to a titanium dioxide surface showed that the lithium

cation is able to annihilate the electric field created by the charge injected on the conduction band of titanium dioxide, a behavior identified with a Stark effect.

A theoretical model [21] employing molecular simulation of the TiO_2 surface attributed the origin of this effect to an electric field generated by a charge in the semiconductor and/or to the presence of the oxidized complex.

A study intending to examine these phenomena by means of a theoretical simulation and TDDFT calculations was performed [22]. It seeked to show that this behavior can be attributed to a dye–lithium adduct that is photochemically generated (Figure 30), and also to look how this adduct influences the photo conversion efficiency of the DSSC. To achieve this goal, the use of BCL methodology and DoLAc architecture is proposed to build a simulation model and calculate its efficiency through the Global Efficiency Index (GEI) with and without Li^+.

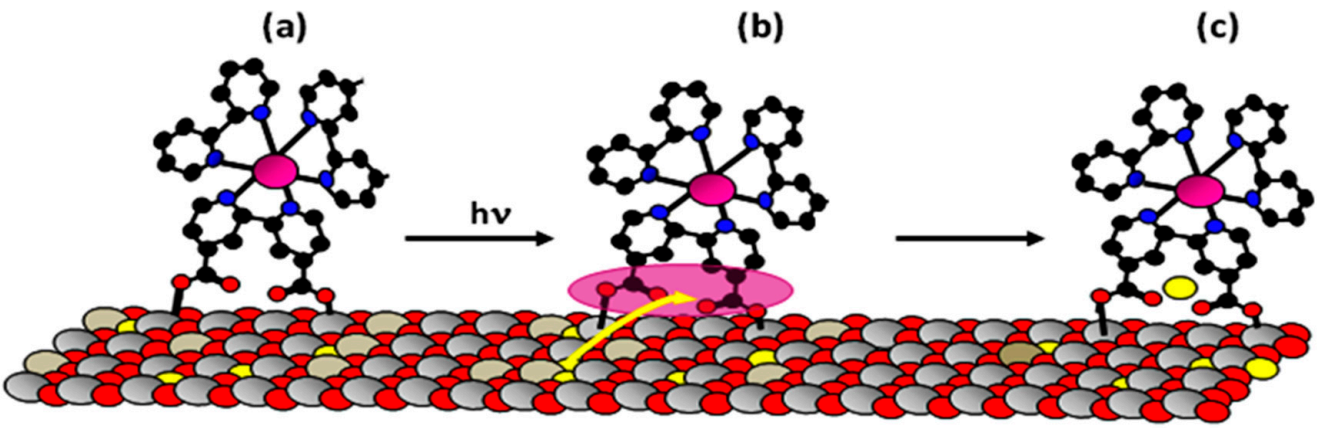

Figure 30. Scheme showing the photochemical generation of the meta-stable lithium adduct. (**a**) Ground state, the ruthenium dye is bound to the surface of TiO_2 (**b**) the excited dye acts as photo-base and captures a Li^+ ion from its neighborhood. (**c**) After deactivation, a Li–dye adduct is formed. Atom color legend: White (Ti), red (O), yellow (Li), black (C), blue (N), and pink (Ru).

7.1. Adduct Generation

At first, a study was carried out to know the interaction between lithium and the Donor-Linker-Acceptor (DolAc) system composed by $[Ru(dmb)_2dcb]$ -$Ti(OH)_3$ in the ground state, according to Equation (36):

$$[Ru(dmb)_2dcb]\text{-}Ti(OH)_3 + Li^+ \rightarrow [Ru(dmb)_2dcb]\text{-}Ti(Li)(OH)_3 \quad (37)$$

After performing a series of geometrical optimizations with the lithium cation in different places of the molecule, the final results always agreed that the most stable structure was with the lithium captured by the $Ti(OH)_3$, which concords with experimental observations.

This result is shown in Figure 31, where it can be seen that through a thermal pathway (path b) an interaction between the complex and the lithium ion does not occur because it is attracted by the oxygen atoms of the $Ti(OH)_3$ group.

The procedure for obtaining the adduct through a photochemical pathway is displayed on Figure 31 through path (a). The optimized structure of the Lithium adduct is obtained through a four steps procedure: first the ground state 1(S0) is optimized. Second, employing this structure as starting geometry, its triplet state is generated and optimized, 1(T1). Through the third step, the Lithium atom is added and the structure with the cation is reoptimized and the new geometry for 1(T1)Li is obtained. In the last step, the multiplicity is changed to singlet and the a new optimization gives the ground state of the metastable adduct $1(S_0)Li$.

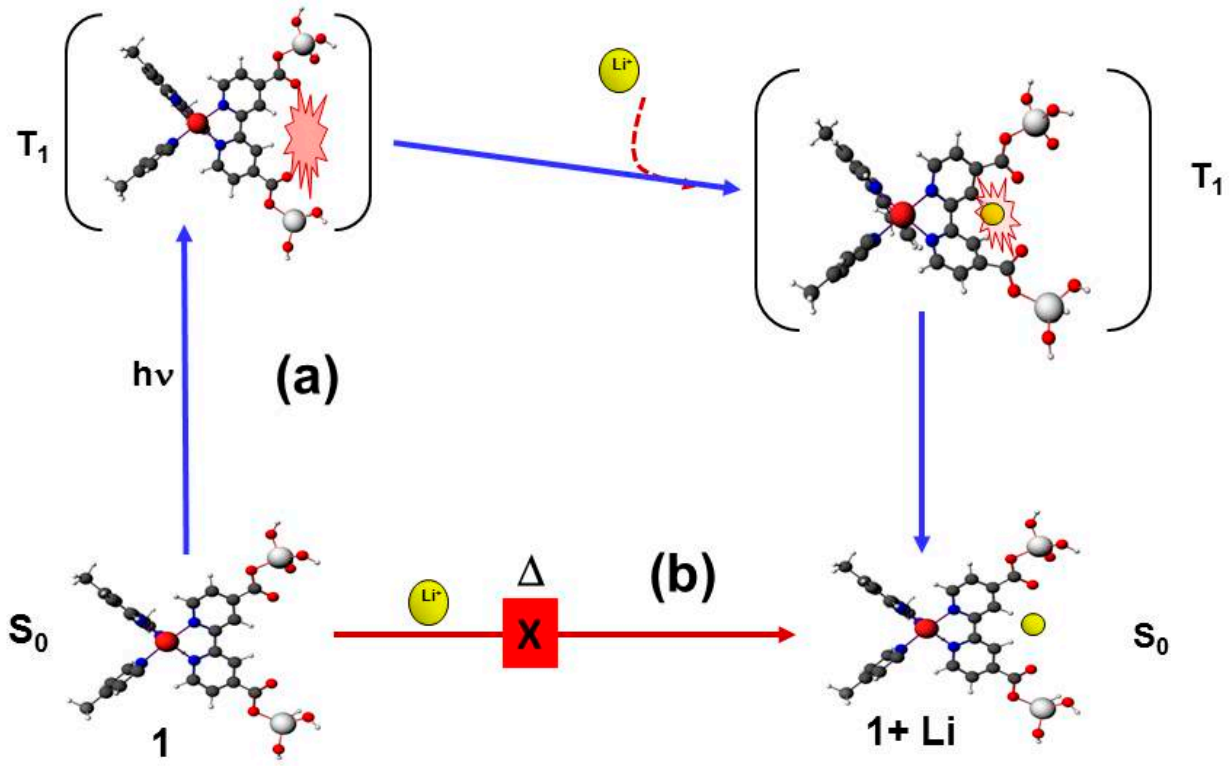

Figure 31. (**a**) Optimization pathway for generation of a dye–lithium–TiO_2 adduct through a triplet state $S_0 \rightarrow T_1 \rightarrow S_0$, sensitization cycle (**b**) Thermal–dark pathway.

7.2. Results

7.2.1. Structure and Geometry

The triplet state of **1** has the special feature that electronic density is concentrated on the carbonyl groups of the dcb ligand. This increase in negative charge on the oxygen atoms generates an electrostatic potential around the carbonyl groups that is capable of attracting small positive charges towards them, as is the case with the lithium ion. Figure 32b displays the structure of the adduct with lithium captured by the carbonyl groups. The calculated atomic distances for d1, d2, d3, d4 and for the twisting angle, α, between the two pyridines rings are displayed on Tables 6 and 7.

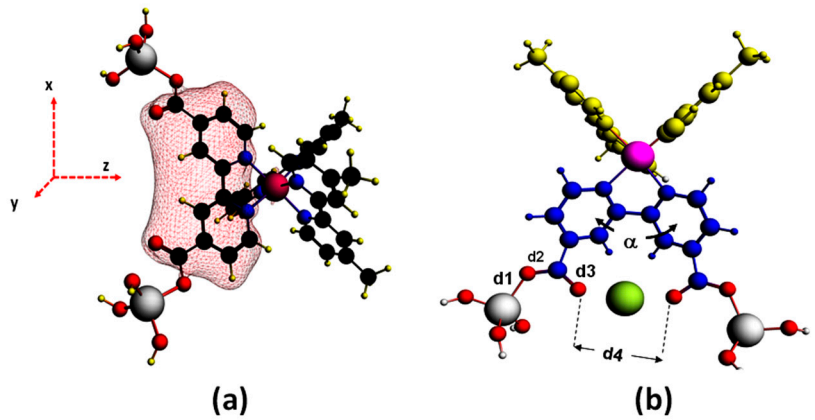

Figure 32. (**a**) Electrostatic potential in complex $1(T_1)$. (**b**) Atomic distances and bond angles for the $1(T_1)$Li.

Table 6. Atomic distances (A) and bond angles (°) for the lithium adduct.

Compound	Ti-O(CO) d1	C-O d2	C=O d3	(CO)O-O(CO) d4	(Py-Py) α
1(S0)	1.99	1.30	1.22	6.11	178
1(T1)	1.99	1.30	1.23	6.23	181
1(T1)Li	2.00	1.28	1.25	3.98	158
1(S0)Li	2.00	1.27	1.25	4.03	161

Table 7. TDDFT results for complexes 1 and 1 + Li.

Compound	Electronic Transition (Γ)	Energy (eV) Exp	Calc	Oscillator Strength	Main Excitation	Nature
1(S0)	1	2.55	2.55	0.05	61% H2 → L2 15% H0 → L3 12% H0 → L2 10% H2 → L1	Ru → dcb Ru → dcb Ru → dmb Ru → dmb
1(S0)Li	1a	2.43	2.44	0.07	59% H2 → L2 26% H0 → L1 6% H0 → L2	Ru → dcb Ru → dmb + dcb Ru → dmb + dcb

An analysis of the results in Table 6 shows that the interaction of lithium with the complex is evidenced in a loss of planarity of the dcbp ligand, which merges from the decrease in the alpha angle between the two pyridine rings, from 178° in the free complex to 161° in the adduct. This distortion in planarity is originated in the triplet state and continues to be present when the system decays to the basal state. A second change that must be considered is the decrease in the distance (d4) between the oxygen of the carbonyls of the dicarboxylate substituents passing from 6.11 Å in the complex to 4.03 Å in the adduct.

The above data are consistent and indicate that the ligand undergoes a type of folding where its molecular structure adopts a shape similar to a vessel, which consequently allows the capture and stabilization of the cation within it.

7.2.2. Molecular Orbitals

Figure 33a shows the energy and composition diagram of the molecular orbitals of the complex and its adduct. To carry out the analysis, the system is described in terms of four fragments: {dmb}, {dcb}, {Ru}, and {$Ti(OH)_3$}. The stabilization of the HOMO and LUMO levels is observed; meanwhile, the LUMO + 1 and LUMO + 2 are not altered. This stabilization produces a decrease in the HOMO–LUMO band gap energy from 2.07 eV to 1.96 eV; it is manifested as a bathochromic shift in the absorption maxima of the MLCT band. The increase in HOMO energy and ionization potential is experimentally correlated with the increase in oxidation potential.

In both cases, in the complex and the adduct, the HOMO and LUMO present the same composition; however, for LUMO + 1 and LUMO + 2, notorious differences appear, as shown in Figure 33b: the dmb fragment predominates in both orbitals in the free complex, but in the adduct the dcb fragment appears with a large contribution. This change in the composition is due to the presence of the Li^+ ion which stabilizes the {dcb} fragment.

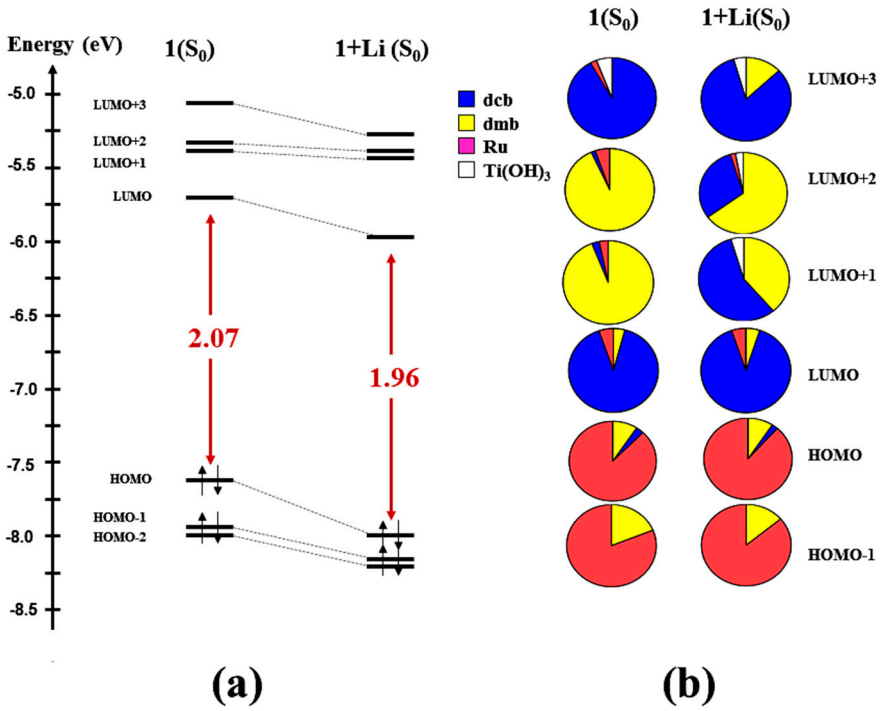

Figure 33. (**a**) Energy levels diagram for the lithium adduct. (**b**) Molecular orbital composition in terms of fragments dcb, dmb, Ru and $Ti(OH)_3$.

7.2.3. Absorption Spectra and Stark Shift

By means of TDDFT calculations the effect of Lithium on the absorption spectrum of the 1S0 complex can be simulated, as shown in Figure 34a. According to these calculations, the complex presents an electronic transition Γ_1 with MLCT character at λ_{max} = 486 nm, which moves up to Γ_{1Li} with λ_{max} = 509 nm when lithium is present.

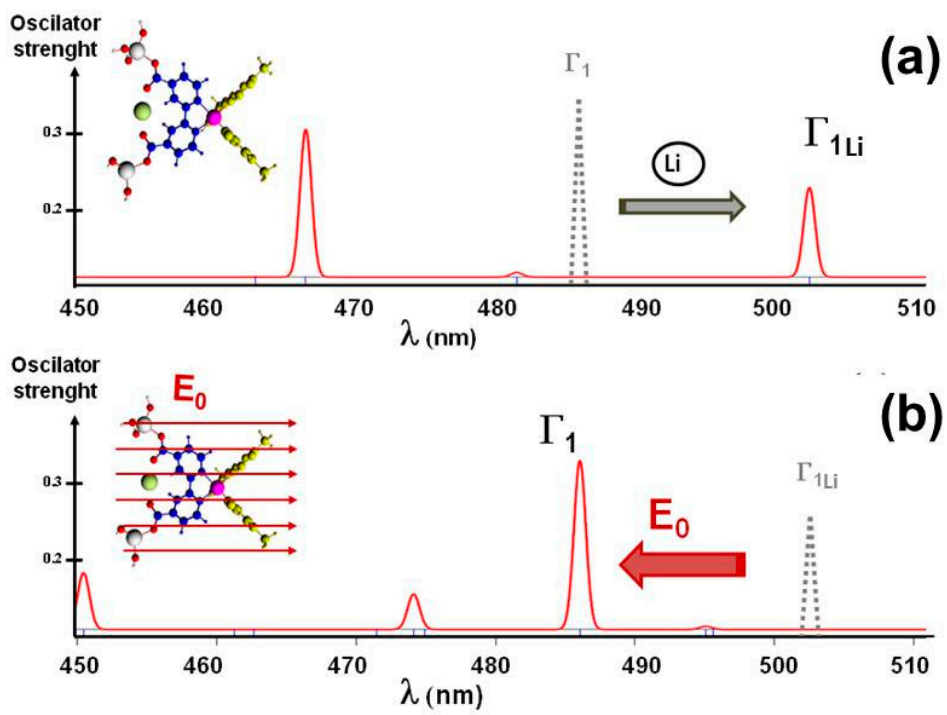

Figure 34. (**a**) Stark effect caused by Li^+ on the Γ1 transition. (**b**) Annihilation of the Stark effect by an external potential of E0.

Table 7 shows the composition of both bands, which are similar since they contain 60% of the same excitation from HOMO-2 to LUMO + 2 (Ru→dcb). The difference between them arises because Γ_1 contains 29% of an excitation between HOMO to LUMO + 2 and LUMO + 3, while Γ_{1Li} only contains 26% of an excitation from HOMO to LUMO + 1. According to this, the 0.11 eV shift on the λ_{max} of the absorption spectra is identified with a Stark effect caused by the electric field of Li^+.

This value is consistent with the 0.12 eV displacement in λmax observed experimentally. Besides the existence of the electronic excitation from HOMO-2 to LUMO previously mentioned, there are also small 10–15% contributions to Γ from the HOMO to the LUMO + 1 and LUMO + 2. The HOMO to LUMO + 3 excitation is present in the free complex but absent in the adduct.

As indicated above, the signal observed at 509 nm is not a new signal but rather a ghost signal, caused by the electric field of lithium, on the initial transition at 489 nm. One way to demonstrate the existence of this field is to neutralize it with a field of the same intensity but in the opposite direction. The bathochromic shift observed on going from 1(S0) to 1(S0)Li can be neutralized (Figure 34b) by applying an electric field pointing to the negative side of the Z-coordinate axis, with a magnitude of EZ = E_0 = 7.3 MV/cm.

This value for the electric field is in good agreement with the 1–10 MV/cm values previously reported for this class of molecules bound to TiO_2. With application of this external field, the transition Γ_{1a} disappears and gives rise to the unshielded transition Γ_1 observed at 489 nm.

7.2.4. Effect on the Performance Index

The main objective of this section is to calculate the effect of lithium on the theoretical index GEI. As mentioned in previous chapters, the global efficiency index is obtained through the product of three local indexes associated with the transmission of the absorbed energy (F1) the injected charge (F2) and the regeneration efficiency (F3).

Table 8 displays the calculated values for the ruthenium dye 1(S0) and the adduct 1(S0)Li. The most important result of this table is that the GEI confirms that the lithium adduct has a higher global efficiency yield than the dye alone. The causes of this increase in efficiency can be determined through the variations of the three indices. First, it can be observed that in the case of the adduct the values of the indices F1 and F3 increase above the values of the free complex. Looking to the enhancement of the energy obtained by light harvesting, it is due to an increase in the energy delivered to the anchor ligand, and because of a greater level of participation from the anchor group.

Table 8. Calculated values for the Global Efficiency Index.

COMPLEX	EA	ED	Φ_t	F1	$\Delta\varepsilon$	ΔV_{DA}	F2	F3	%GEI *
1(S0)	0.96	0.36	0.06	**0.021**	1.31	−0.26	**0.12**	**4.43**	**0.27**
1(S0)Li	0.94	0.46	0.08	**0.037**	0.83	−0.14	**0.07**	**5.64**	**0.35**

(*) %GEI = $F_1F_2F_3$/Esun, Esun = 4.13 eV.

The second indexes measuring the amount of charge injected diminishes because the SOMO orbital is stabilized, and the energy gradient is lower.

In the previous analysis of molecular orbital energies, it was mentioned that the presence of lithium causes an increase in the oxidation potential of ruthenium dye. The enhancement of the redox potential caused by the absorption of lithium on the surface of the dye could lead to a pseudo-capacitance effect [23,24] which increases the current transport and favors the regeneration process.

According to the value of the GEI displayed in the last column of Table 8, it can be concluded that the presence of the metastable Li–adduct has a positive impact on the Global Efficiency Index, which can be related to a higher value of the PCE of the cell, caused mainly

by two factors: a more efficient harvesting of sunlight energy, and a faster regeneration of the starting photo catalyst.

8. Improvement of the Performance of N3 with a Mono Carboxylate Ligand

The development and the improvement of new dyes for sensitized solar cell in order to increase their efficiency require the knowledge of several types of processes occurring during the operation of the cell [25].

The electron transfer between the dye and the semiconductor is one the key process participating in the photocatytic cycle and involves electron transfer from the dye to the semiconductor through the anchor ligand, which acts as a molecular bridge, transferring electronic density among both species. In principle, the anchoring ligand accomplishes two functions: it acts as physical linker between the dye and the surface of the semiconductor, as well as participating in the electron injection process through the carboxylic group.

The structure of a typical dye sensitized solar cell follows the general type of donor–linker–acceptor architecture; in this case, the donor is located on the ruthenium complex, the linker is the dicarboxy–bipyridine ligand, and the acceptor is titanium dioxide. Interaction occurs when the ruthenium dye absorbs energy from sunlight spectra reaching a transient excited state, through which it is able to transfer energy to the acceptor group, composed mainly by empty orbitals with a metallic character.

According to the BCL scheme, the energy absorbed by the ruthenium dye is delivered to the anchor ligand; this process is followed by an intersystem crossing to reach a triplet state, where the electronic density is concentrated on the carboxylic moiety and becomes available for injection. In this sense carboxyl groups can act as discharge points for the energy concentrated on the anchor ligand to be transferred to the surface of the acceptor.

For the case of ruthenium-based DSSC, two types of anchor ligands (Figure 35) that have been successfully employed are 4,4dicarboxibipyridine (dcbp) and tricarboxiterpiridine (tctp). When these types of ligands form ruthenium dyes that additionally incorporate thiocianate as donor group, high values of photoconversion efficiency have been observed.

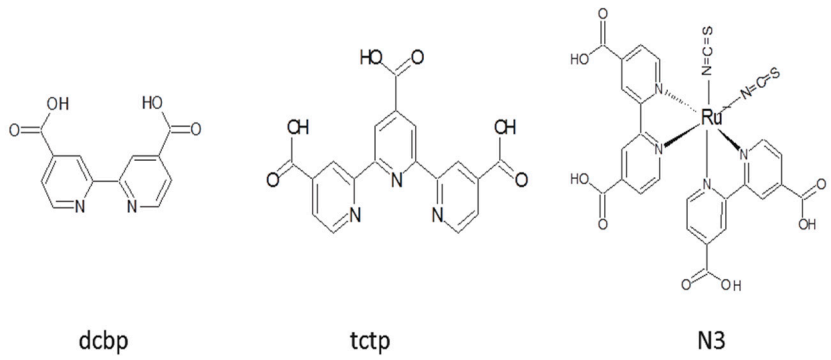

Figure 35. Dcbp, tctp, and N3 dye.

The use of these types of organic molecules as anchor ligands has been very exhaustive and has given rise to a series of ruthenium complexes with thiocyanate as donor booster, that have been very successful in terms of efficiency, measured under standard conditions. In particular, the homoleptic $[Ru(SCN)_2(dcbp)_2]^{+2}$, also labeled as N3, has been extensively studied, and its photoconvertion efficiency measured under standard conditions is 7.1%.

Phenylpiridine (pp) ligand (Figure 36) has been reported to be a useful ancillary ligand to replace tyocianate and provide a new family of ruthenium dyes with a high-efficiency yield. This ligand accomplishes two important functions: to act as an electron donor and stabilize the oxidized dye after electron injection, and to cause a red shift of the absorption spectra. The participation of the pp ligand in the molecular orbital composition is mainly at the HOMO level. The mono carboxylate version (mcpp) displays rather different behavior [26], since the symmetry of the ligand is broken with the presence of

the carboxy moiety on the pyridine ring, causing its decomposition in two fragments: one located in the HOMO and the other in the LUMO, through which electron injection occurs.

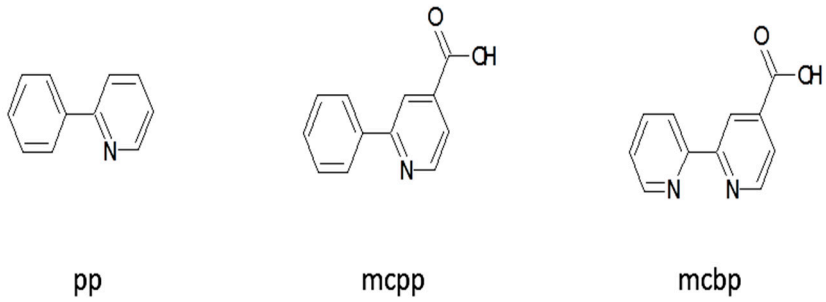

Figure 36. Pp, mcpp, mcbp.

Analogous with mcpp, bicyclic monocarboxylated ligands derived from bipyridine can be visualized. Nevertheless, it is interesting to note that the countertype of this complex—the monocarboxylated version, mcbp—has not yet been synthesized, although there attempts have been carried out [27].

From a molecular design point of view, the study of this type of ligand is attractive in order to determine if the energy available to be injected into the acceptor group is affected by the number of carboxyl groups present in the anchor ligand [28]. In principle, the energy delivered to the anchor ligand by the chromophore must be transmitted to the acceptor group through the carboxyl groups, and it is worth wondering if it is more efficient for this energy to be delivered through a one-carboxyl group instead of two-carboxyl groups.

Within this context, the present study seeks to calculate, using the BCL methodology, what would be the hypothetical performance index of the complex $[Ru(SCN)_2(mcbp)_2]^{+2}$, (N3mcp2), using the GEI as a predictor for its photo conversion efficiency. As mentioned earlier in this work, the GEI general value is the product of three independent indexes, namely, F1, F2, and F3, that represent the value for the efficiency of light harvesting, electron injection, and regeneration, respectively. According to the model, the F1 parameter is the available energy for injection, which takes into account the amount of absorbed energy from sunlight that finally reaches the anchor group. The F2 parameter represents the amount of energy that is effectively transferred to the acceptor group ($Ti(OH)_3$). The third index measures the ability of the reductor agent (I^-) to regenerate the oxidized dye.

8.1. Method

8.1.1. Molecular Design

The study of the changes occurring in the values of the F1, F2, and F3 parameters when only the one-carboxylate anchor group is present, compared to the disubstituted ligand, would reveal how relevant is the influence of a second moiety for the overall process. To achieve this feature, a comparative study with a set of four complexes containing bi- and mono-carboxylate bipyridine ligands with different binding modes (bridging, unidentate, and bidentate) [29,30] was performed. In Figure 37, four donor–linker–acceptor (DoLAc) structures are displayed; the donor is $[Ru(SCN)_2]$, while the linker is the 1carboxylate ligand bound to the acceptor group $[Ti(OH)_3]$. In the figure, four different types of connections are proposed between the anchor ligand and the acceptor group. The purpose of this series is to examine how the binding mode between the acceptor and the anchor ligand influences the overall result. The homoleptic N3 dye containing two dcbp ligands can be bound to the surface of the semiconductor by means of one anchor ligand (N3bcp1) or by two (N3bcp2). The same possibilities can be observed when monocarboxilate anchor ligands are employed and unidentate mode (N3mcp1) or bidentate (N3mcp2) are expected.

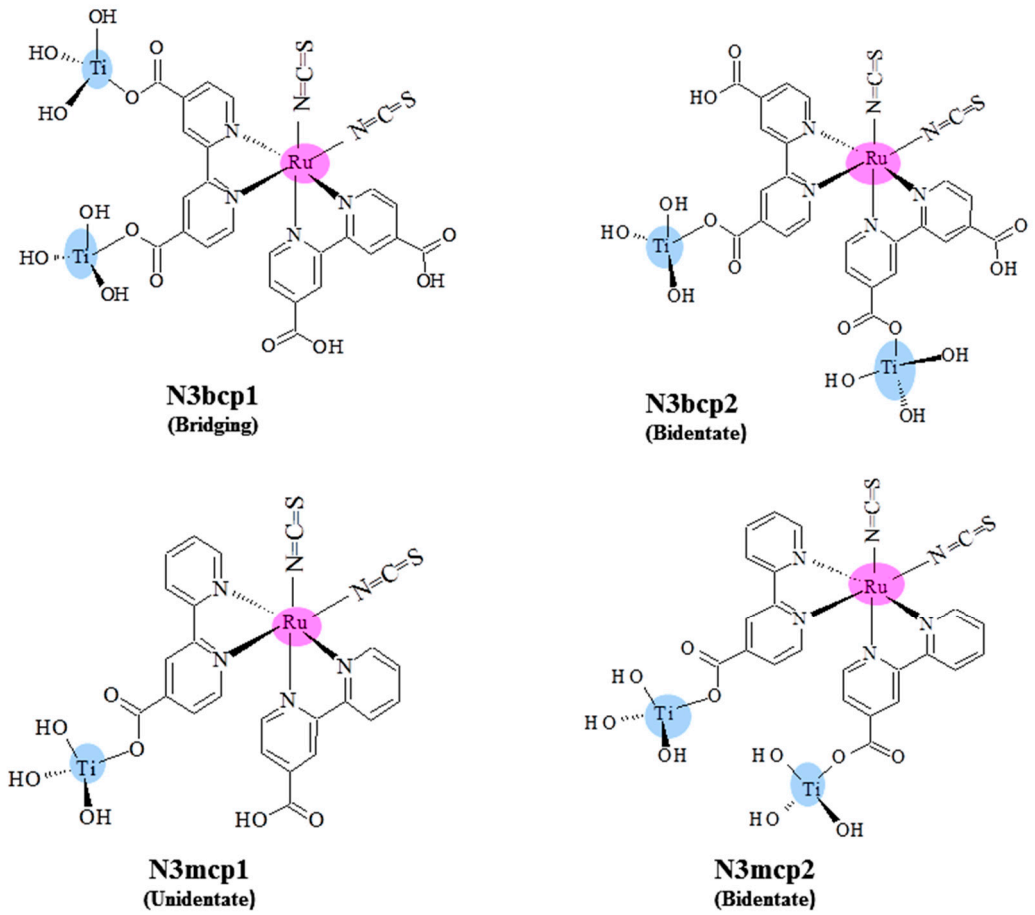

Figure 37. DoLAc structure for the N3 mono a di carboxi complex showing three binding modes.

8.1.2. Computationals Details

Calculations were performed using the ADF package. Geometrical optimization for the ground state and the first triplet were carried out with the OPBE exchange correlation functional. For the TDDFT result, charge analysis and one electron properties the SAOP exchange correlation potential was employed.

8.2. Results

The results for the four complexes are summarized in Table 9. The last column of this table displays the final value for the Global Efficiency Index (GEI), obtained as the product of F1, F2, and F3, divided by E_{SUN}, which is the total energy received from the Sun. Column two and three display the different components involved in the calculation of light-harvesting capacity (see Section 4): absorbed energy (EA), delivered energy, (ED) and composition of the triplet state (Φ_t).

Table 9. Calculated values for the Global Efficiency Index, F1, F2, and F3.

COMPLEX	EA	ED	Φ_t	F1	F2	F3	%GEI *
N3bcp1	0.91	0.59	0.12	**0.069**	**0.124**	**3.059**	**0.64**
N3bcp2	0.81	0.76	0.10	**0.074**	**0.124**	**3.034**	**0.68**
N3mcp2	0.61	0.56	0.15	**0.084**	**0.134**	**2.915**	**0.80**
N3mcp1	0.73	0.29	0.05	**0.015**	**0.140**	**2.633**	**0.13**

(*) %GEI = $100F_1F_2F_3$/Esun (Esun = 4.13 eV).

A first result of the GEI analysis indicates that, in the case of the bisubstituted bipyridine ligand, the method can differentiate between two binding modes: the bridging mode

of N3bcp1, where the two binding positions come from the same bpy ligand; and the bidentate mode of N3bcp2, where the carboxi anchors come from different bpy ligands. The increase in overall efficiency is from 0.64% in the first to 0.68% in the latter.

This increase of 0.4% in efficiency occurring in the bidentate mode can be attributed to an increase in the ability to transmit and deliver light energy: the N3bcp1 absorb more sunlight energy, (0.91 eV), but the fraction of it that reaches the anchor ligand, is greater in the bididentate mode (0.76 eV).

When comparing the Global Efficiency Index of complexes with the same bonding mode as N3bcp2 and the monocarboxylate equivalent ligand, N3mcp2, an increase from 0.68% to 0.80% is observed for the latter. This greater efficiency is located in the light-harvesting energy because the greater participation of the anchor group in the triplet state.

The monocarboyilate complex absorbs less energy from the sunlight spectra than the di carboxylate counterpart; its capacity to deliver energy to the anchor ligand is lesser, but these effects are completely compensated by a 50% increase in the participation of the anchor group on the triplet state and the F1 parameter raises from 0.074 to 0.084. In this sense, it can be concluded that the second carboxylic group on the bipyridine ligands has no effect on the energy delivery capacity of the corresponding ruthenium complex.

It is interesting to examine the increase in the electron injection efficiency which can be understood in collaboration with Figure 38a. The SOMO of the monocarboxylated complex is destabilized according to this scheme resulting in a higher electron gradient ($\delta\varepsilon$) potential and higher F2 value.

The GEI dramatical drops on going from the bidentate mode of N3mcp2 to the monodotentate N3mcp1 with respect to N3mcp2 has its origin in the two factors F1 and F3. For the first index, the light-harvesting energy is strongly reduced because the participation of the anchor group in the triplet state is poor because there is only one point of contact with the semiconductor acceptor group.

The second index, F2, however, slightly increases, driven by the destabilization of the SOMO that enhances the electron injection gap ($\delta\varepsilon$) respect to the LUMO of $Ti(OH)_3$. The HOMO is also destabilized but, in this case, its lower values reduce the energy gradient (ΔE) with respect to the HOMO of Iodide and the regeneration index (F3) is lowered as shown in Figure 38a.

The transition density analysis (TDA), Section 3.2, for the four LUMOs is displayed in Figure 38b. The population of the set of LUMOs with the energy captured from the absorption process generates a transient density that is distributed along the different fragments composing the molecular orbital. In this figure, it is clearly demonstrated how complexes in the bidentate binding mode, the transition density is equally distributed for all the anchor ligand. In the other two modes, unidentate and bridging, part of the absorbed energy is directed towards the ancillary ligand and not towards the anchor and a lost in the overall yield is caused.

As a whole, the present study confirms the result of previous [31] calculations that indicate the increase in the photo conversion efficiency in homoleptic ruthenium complexes with thiocyanate when the monocarboxybipyridine anchor ligand is used instead of the dicarboxylated.

The results show that ruthenium complexes with a monocarboxylated ligand could present two binding modes: unidentate and bidentate. The unidentate mode occurs when the homoleptic complex binds to the surface by means of one anchor ligand. The other ligand, which is not bound to the semiconductor, acts as an ancillary ligand. In the bidentate mode, the complex binds to the surface with two contact points, coming from the two anchor ligands.

According to our calculations, the bidentate mode displays a higher value of photo-conversion efficiency (0.80) than the monodentate (0.13) and the bridging (0.64).

Comparing complexes in the bidentate binding, in the monocarboxylate complex (N3mcp2) the GEI value shows an increment in regard to the latter (N3bcp2), from 0.68 to

0.80, could result in the increment of the PCE of N3 from 7.1 to 7.6%. This increase of 0.5% in the overall yield is of a similar magnitude to that registered in the complex with carboxy pyridyl quinoline, whose yield increases by 0.3% [32].

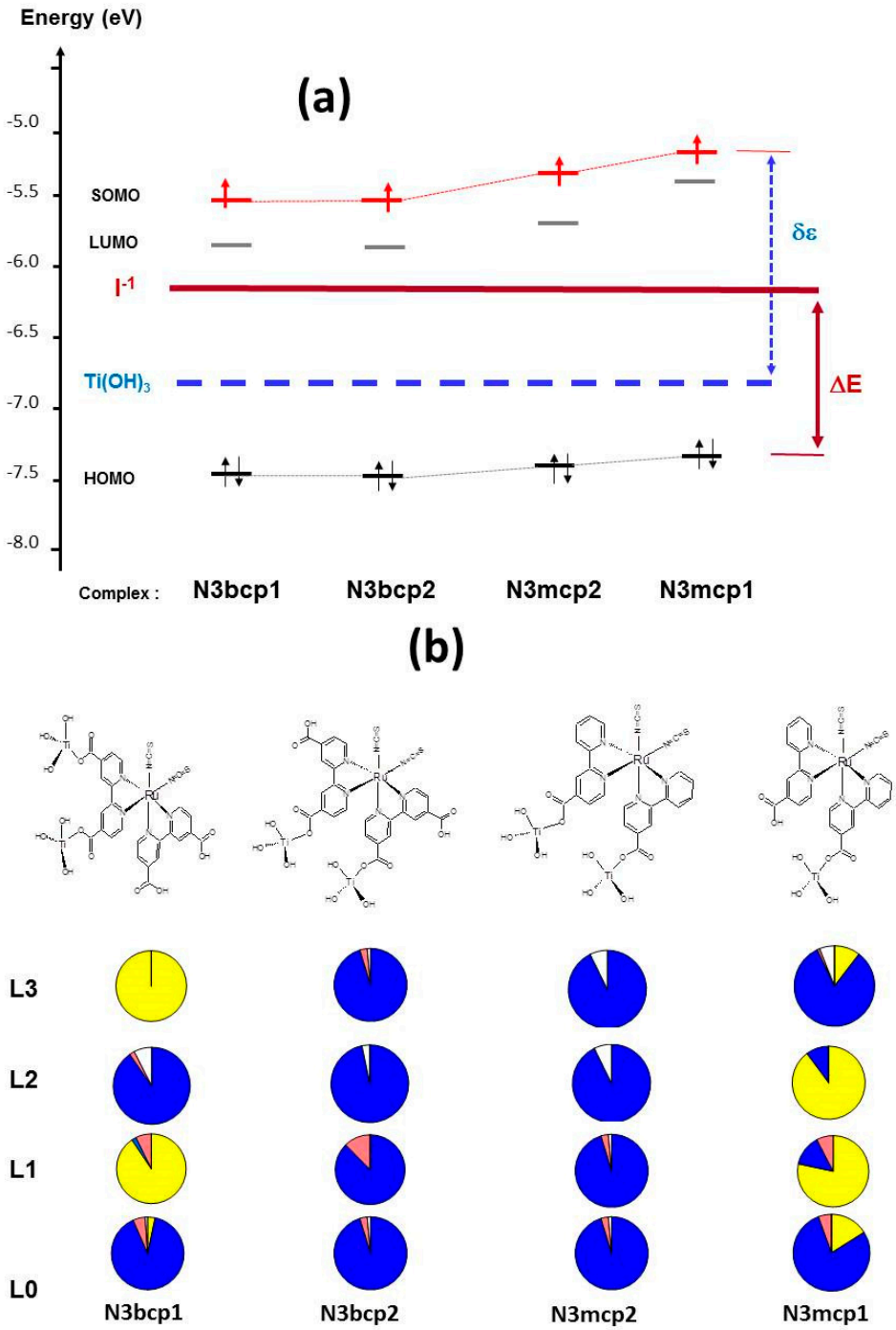

Figure 38. (**a**) Molecular orbital energies scheme. (**b**) Transition density analysis (yellow: ancillary ligand, blue: anchor ligand, pink: ruthenium, white: acceptor).

In summary, the BCL method was employed to gain more insight in the role of the anchor ligand, and the number of anchoring groups, in the overall yield of ruthenium–thiocyanate-based dyes. The method predicts that a ruthenium complex with monocarboxylated ligands is more efficient than a similar complex with dicarboxylic ligands.

Author Contributions: Conceptualization, M.B.; methodology, M.B., I.C. and B.L.; formal analysis, M.B., I.C. and B.L.; writing—original draft preparation, M.B., I.C. and B.L.; writing—review and editing, M.B., I.C. and B.L.; supervision, M.B.; funding acquisition, M.B., I.C. and B.L. All authors have read and agreed to the published version of the manuscript.

Funding: The initial part of this work was funded through the Chilean research agency Fondecyt, through Projects No. 1020517, 7070181and 1070799. The second part received no external funding.

Acknowledgments: The authors acknowledge former graduate and undergraduate students for their unvaluable contribution to this work. Collaborations with Faculty members of national and international universities, cited in the different references, were crucial to make this review possible. One of us (MB) acknowledges the scientific inspiration received by Fernando Zuloaga (RIP) at the first stages of his career.

Conflicts of Interest: The authors declare no conflict of interest.

References

1. O'Regan, B.; Grätzel, M. A low-cost, high-efficiency solar cell based on dye-sensitized colloidal TiO_2 films. *Nature* **1991**, *353*, 737–740. [CrossRef]
2. Aghazada, S.; Nazeeruddin, M. Ruthenium Complexes as Sensitizers in Dye-Sensitized Solar Cells. *Inorganics* **2018**, *6*, 52. [CrossRef]
3. Nazeeruddin, M.; Péchy, P.; Renouard, T.; Zakeeruddin, S.M.; Humphry-Baker, R.; Comte, P.; Liska, P.; Cevey, L.; Costa, E.; Shklover, V.; et al. Engineering of efficient panchromatic sensitizers for nanocrystalline TiO_2-based solar cells. *J. Am. Chem. Soc.* **2011**, *123*, 1613–1624. [CrossRef]
4. Green, M.; Dunlop, E.; Hohl-Ebinger, J.; Yoshita, M.; Kopidakis, N.; Ho-Baillie, W.Y. Solar Cell Efficiency Tables (Version 55). *Prog. Photovolt.* **2020**, *28*, 3–15. [CrossRef]
5. Arias, M.; Concepción, J.; Crivelli, I.; Delgadillo, A.; Díaz, R.; François, A.; Gajardo, F.; López, R.; Leiva, A.M.; Loeb, B. Influence of Ligand Structure and Molecular Geometry on the Properties of d^6 Polypyridinic Transition Metal Complexes. *Chem. Phys.* **2006**, *326*, 54–70. [CrossRef]
6. Norambuena, E.; Olea-Azar, C.; Delgadillo, A.; Barrera, M.; Loeb, B. Comparative evaluation of the acceptor properties of quinone derivatized polypyridinic ligands. *Chem. Phys.* **2009**, *359*, 92–100. [CrossRef]
7. Gajardo, F.; Barrera, M.; Vargas, R.; Crivelli, I.; Loeb, B. Influence of the Nature of the Absorption Band on the Potential Performance of High Molar Extinction Coefficient Ruthenium(II) Polypyridinic Complexes as Dyes for Sensitized Solar Cells. *Inorg. Chem.* **2011**, *50*, 5910–5924. [CrossRef]
8. François, A.; Díaz, R.; Ramírez, A.; Loeb, B.; Barrera, M.; Crivelli, I. Evaluation of the potential effectiveness of Ruthenium(II) complexes with 2,3-disubtituted pyrazino[2,3-f][1,10]phenanthroline anchors, R_2ppl (R = CN, COOH, COOEt, OH) as sensitizers for solar cells. *Polyhedron* **2013**, *52*, 62–71. [CrossRef]
9. Te Velde, G.T.; Bickelhaupt, F.M.; Baerends, E.J.; Fonseca Guerra, C.; van Gisbergen, S.J.; Snijders, J.G.; Ziegler, T. Chemistry with ADF. *J. Comput. Chem.* **2001**, *22*, 931–967. [CrossRef]
10. Parr, R.; Szentpaly, L.; Liu, S.J. Electrophilicity Index. *J. Am. Chem. Soc.* **1999**, *121*, 1922–1944. [CrossRef]
11. Fukui, F. Role of frontier orbital in chemical reactions. *Science* **1982**, *218*, 747–754. [CrossRef] [PubMed]
12. Bruker. *Bruker Win-EPR System. Bruker–Franzen Analytik 6 mbH*; Version 2.11; Copywrite 1990–1996; Bruker: Billerica, MA, USA, 1995.
13. Grätzel, M. The Advent of Mesoscopic Injection Solar Cells. *Prog. Photovolt Res. Appl.* **2006**, *14*, 429–444. [CrossRef]
14. Beer, P.D.; Kocian, O.; Mortimer, R.J.; Ridgway, C. New alkynyl- and vinyl-linked benzo- and aza-crown etherbipyridyl ruthenium(II) complexes which spectrochemically recognize Group IA and IIA metal cations. *J. Chem. Soc. Dalton Trans.* 1993, pp. 2629–2638. Available online: https://fdocuments.net/document/new-alkynyl-and-vinyl-linked-benzo-and-aza-crown-etherbipyridyl-rutheniumii.html?page=3 (accessed on 24 November 2021).
15. Cook, M.J.; Lewis, A.P.; McAuliffe, G.S.G.; Skarda, V.; Thomson, A.J.; Glasper, J.L.; Robbins, D.J. Luminescent metal complexes. Part 1. Tris-chelates of substituted 2,2′-bipyridyls with ruthenium (II) as dyes for luminescent solar collectors. *J. Chem. Soc., Perkin Trans II*. 1984, pp. 1293–1301. Available online: https://www.semanticscholar.org/paper/Luminescent-metal-complexes.-Part-1.-Tris-chelates-Cook-Lewis/8a945b0317d7f4923bf76ae789d0f6b6c2bd126a (accessed on 24 November 2021).
16. Song, L.G.; Feng, J.; Wang, X.-S.; Yu, J.-H.; Hou, Y.-J.; Xie, P.-H.; Zhang, B.-W.; Xiang, J.-F.; Ai, X.-C.; Zhang, J.P. Dual Emission from 3MLCT and 3ILCT Excited States in a New Ru(II) Diimine Complex. *Inorg. Chem.* **2003**, *42*, 3393–3395. [CrossRef] [PubMed]
17. Han, X.; Wu, L.-Z.; Si, G.; Pan, J.; Yang, Q.-Z.; Zhang, L.-P.; Tung, C.-H. Switching between Ligand-to-Ligand Charge-Transfer, Intraligand Charge-Transfer, and Metal-to-Ligand Charge-Transfer Excited States in Platinum(II) Terpyridyl Acetylide Complexes Induced by pH Change and Metal Ions. *Chem. Eur. J.* **2007**, *13*, 1231–1237. [CrossRef] [PubMed]
18. Barrera, M.; Crivelli, I.; Loeb, B. On the performance of ruthenium dyes in dye sensitized solar cells: A free cluster approach based on theoretical indexes. *J. Mol. Model.* **2016**, *22*, 118. [CrossRef]

19. Green, M.; Dunlop, E.; Hohl-Ebinger, J.; Yoshita, M.; Kopidakis, N.; Hao, X. Solar cell efficiency tables (version 57). *Prog. Photovolt Res. Appl.* **2021**, *29*, 3–15. [CrossRef]
20. Staniszewski, A.; Ardo, S.; Sun, Y.; Castellano, F.; Meyer, G. Slow Cation Transfer Follows Sensitizer Regeneration at Anatase TiO_2 Interfaces. *J. Am. Chem. Soc.* **2008**, *130*, 11586–11587. [CrossRef]
21. Pastore, M.; De Angelis, P. Computational Modeling of Stark Effects in Organic Dye-Sensitized TiO_2 Hetero interfaces. *J. Phys. Chem. Lett.* **2011**, *2*, 1261–1267. [CrossRef]
22. Barrera, M.; Ardo, S.; Crivelli, I.; Loeb, B.; Meyer, G.J. The role of lithium cations on the photochemistry of Ruthenium complexes in dye-sensitized solar cells: A TDDFT study with the BCL model. *J. Photochem. Photobiol. A.* **2018**, *364*, 510–515. [CrossRef]
23. Liu, J.; Wang, J.; Xu, C.; Jiang, H.; Li, C.H.; Zhang, L.; Lin, J.; Shen, Z.X. Advanced Energy Storage: Basic Principles, Analytical Methods, and Rationale Material Design. *Adv. Sci.* **2018**, *5*, 1700322. [CrossRef]
24. Liang, X.; Liu, L.; Cai, G.; Yang, P.; Pei, Y.; Liu, C. Evidence for Pseudocapacitance and Faradaic Charge Transfer in High-Mobility Thin-Film Transistors with Solution-Processed Oxide Dielectrics. *J. Phys. Chem. Lett.* **2020**, *11*, 2765–2771. [CrossRef] [PubMed]
25. Ardo, S.; Meyer, G.J. Photodriven heterogeneous charge transfer with transition-metal compounds anchored to TiO_2 semiconductor surfaces. *Chem. Soc. Rev.* **2009**, *38*, 115–164. [CrossRef] [PubMed]
26. Iturbe, C.; Loeb, B.; Barrera, M.; Brito, I.; Cañete, A. Design and synthesis of non-symmetric phenylpyridine type ligands. Experimental and theoretical studies of their corresponding iridium complexes. *Polyhedron* **2016**, *118*, 159–170. [CrossRef]
27. Hewat, T.; McDonald, S.; Lee, J.; Rahman, M.; Cameron, P.; Hu, F.-C.; Chi, Y.; Yellowlees, L.J.; Robertson, N. Varying numbers and positions of carboxylate groups on Ru dyes for dye-sensitized solar cells: Uptake on TiO_2, cell performance and cell stability. *RSC Adv.* **2014**, *4*, 10165–10175. [CrossRef]
28. Islam, A.; Sugihara, H.; Arakawa, H. Molecular design of Ruthenium(II) polypyridyl photosensitizers for efficient nanocrystalline TiO_2 solar cells. *J. Photochem. Photobiol. A* **2003**, *158*, 131–138. [CrossRef]
29. Kilså, K.; Mayo, E.; Brunschwig, B.; Gray, H.; Lewis, N.S.; Winkler, J.R. Anchoring Group and Auxiliary Ligand Effects on the Binding of Ruthenium Complexes to Nanocrystalline TiO_2 Photoelectrodes. *J. Phys. Chem. B* **2004**, *108*, 15640–15651. [CrossRef]
30. Koposov, A.Y.; Cardolaccia, T.; Albert, V.; Badaeva, E.; Kilina, S.; Meyer, T.J.; Tretiak, S.; Sykora, M. Formation of assemblies comprising Ru-polypyridine complexes and CdSe nanocrystals studied by ATR-FTIR spectroscopy and DFT modeling. *Langmuir* **2011**, *27*, 8377–8383. [CrossRef]
31. Barrera, M. The BCL Approach for the Molecular Design of New Ruthenium Complexes for Dye Sensitized Solar Cells. *J. Anal. Pharm. Res.* **2017**, *1*, 4–6.
32. Yanagida, M.; Yamaguchi, T.; Kurashige, M.; Fujihashi, G.; Hara, K.; Katoh, R.; Sugihara, H.; Arakawa, H. Nanocrystalline solar cells sensitized with monocarboxyl or dicarboxyl pyridylquinoline ruthenium(II) complexes. *Inorg. Chim. Acta* **2003**, *351*, 283–290. [CrossRef]